ON METASTABLE NITRIDES WITH POTENTIAL RENEWABLE ENERGY APPLICATIONS

by

Christopher Michael Caskey

A thesis submitted to the Faculty and the Board of Trustees of the Colorado School of Mines in partial fulfillment of the requirements for the degree of Doctor of Philosophy (Applied Chemistry)

Golden, Colorado

August 25, 2014

Signed: _____
Christopher M. Caskey

Signed: _____
Dr. Ryan M. Richards
Thesis Advisor

Golden, Colorado

August 25, 2014

Signed: _____
Dr. David Wu
Professor and Head
Department of Chemistry and Geochemistry

To:

My parents

TABLE OF CONTENTS

LIST OF FIGURES

CHAPTER 1 INTRODUCTION TO THESIS

Background and significance

The progress of civilization and the quest for low-pollution energy sources[1,2] produces new applications for materials which must be met by the creation of new materials or the application of existing materials to new roles. Metastable nitride semiconductors are set of materials where known materials have not yet been matched to applications and unknown materials await discovery. This dissertation seeks to match known materials to applications while discovering new materials and measuring their properties.

Metal nitrides are interesting materials because the nitrogen can behave in a manner characteristic of neighboring elements in the periodic table (oxygen and carbon),[3] leading to a wide variety of current and future applications.[4] For example, titanium nitride (TiN) is similar to titanium carbide in its structure and conductivity. TiN has been investigated for its catalytic properties[5] and used commercially for it wear resistance.[6] Nitrides can also be oxide-like, running the spectrum from the ionic Li_3N to the covalent Si_3N_4.[3] The oxide-like nitrides include many semiconductors, and the group III nitrides are well studied and include materials such as GaN, InN, and AlN which have been used in photovoltaic systems and in light emitting diodes (LEDs).[4,7] Only more recently have nitride materials outside of the group III nitrides been explored for optoelectronic applications. The covalent copper nitride (Cu_3N) has recently been predicted to possess electronic tolerance to physical defects,[8] Ta_3N_5 has been used an absorber in water-splitting applications,[9] and alloys of the group IV spinel nitrides have been proposed as LED materials with tunable band gaps.[10]

This thesis explores some of the lesser-studied materials in the metal nitride family, copper nitride (Cu_3N), two tin nitrides (Sn_3N_4 and $SnN_{1-\delta}$) and antimony oxynitride, via high-throughput combinatorial methods.

High-throughput combinatorial experiments provide a wide range of compositions and synthesis conditions which allow the scientist to rapidly optimize a property or set of properties in a materials family,[11,12] or to explore synthesis space for unreported compounds.[13] Our current implementation of high-throughput materials science involves three steps: 1) Producing thin film samples with spatial gradients in composition or growth conditions, 2) Measuring the properties

of these samples at spatially resolved points on the sample, and 4) processing the resultant data in a semi-automated manner.

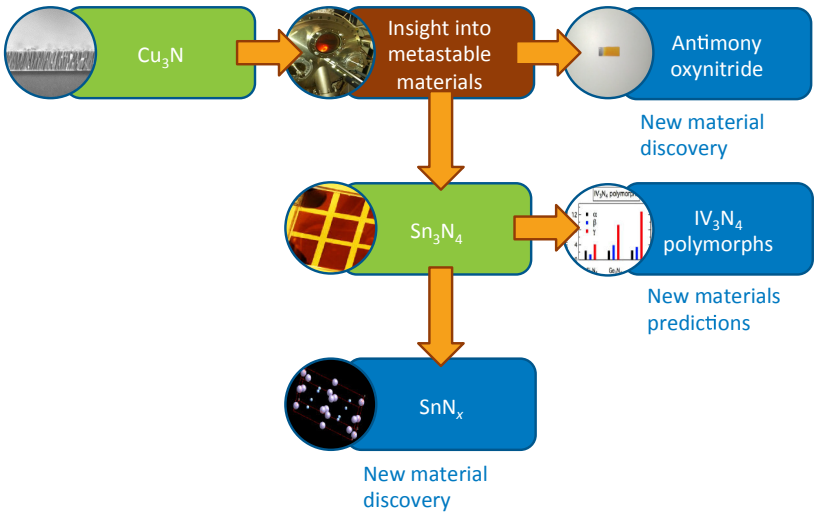

Fig. 1.1: Visual outline of thesis

Thesis organization

This thesis is organized into six chapters. The present chapter is Chapter 1, which contains the introduction, a background of the field, and summaries of the individual chapters.

Chapter 2 is published in *Materials Horizons* and focuses on copper nitride and the chemical potential of nitrogen. Because copper nitride is a thermodynamically metastable material, highly reactive species are required for its synthesis. This chapter evaluates the potential for energy conversion applications of copper nitride, a rather unexplored simple binary metastable nitride semiconductor. Studying copper nitride in the context of solar energy conversion applications provides a conceptual advance in the field of optoelectronic nitride semiconductors, a field that so far has been limited to group III nitrides. Further, shown herein is a high-throughput method for varying the activity of the anion during sputtering. The high-throughput variation of nitrogen activity demonstrated in this chapter represents a readily applicable advance in the field of combinatorial materials science, which to date primarily focused on varying cation composition. Finally, this work provides a framework for evaluating the likelihood of synthesizing other non- equilibrium materials. The rationalization of the thermodynamic metastability of the copper nitride material in terms of its convex hull and atomic

nitrogen chemical potential is a conceptual insight in the field of materials-by-design, in particular computational materials prediction, and was extended to the nitrides of tin, antimony, and bismuth.

Chapter 3 focuses on the previously known binary tin nitride Sn_3N_4 and its group IV nitride relatives. We report a study of the semiconducting properties tin nitride by theory and experiment, and a computational study of related group IV nitride polymorphs. Thin film synthesis was accomplished by high-throughput reactive sputtering, and DFT+GW and DFT slab calculations were used to explore the electronic structure. For tin nitride, we find a band gap of 1.54 eV and predict a large hole effective mass and a small electron effective mass. Periodic and structural trends in electrical properties are observed in the IV_3N_4 polymorphs. The results provide insight into the solid-state chemistry of the materials family and suggest that tunable semiconducting properties may be available in the group IV nitride alloys.

Chapter 4 extends the work of Chapter 2 to tin nitride. We demonstrated for Cu_3N that simultaneous modulation of substrate temperature and target-substrate distance allows facile exploration of temperature-pressure phase space. This phase space can also be thought of as the growth conditions in terms of production of more oxidized or more reduced films. Until now, crystalline tin nitride has only been observed in its fully oxidized Sn(IV) form: the spinel Sn_3N_4. Utilizing anion chemical potential modulation developed in Chapter 2, we explored conditions more reducing than those needed to produce Sn_3N_4. By decreasing the nitrogen chemical potential using the pressure (target-substrate distance) variable, we synthesized an amorphous analogue of the Sn_3N_4 spinel, which is known in the literature to be a slightly reduced compared to the ideal Sn_3N_4. By reducing the chemical potential of nitrogen using the temperature variable, we synthesized a crystalline $SnN_{1-\delta}$ compound, which likely contains Sn(II) and Sn(IV) species. The discovery of a novel, binary, semiconductor composed of Earth-abundant elements at mild synthesis conditions is exciting for two reasons. First, it demonstrates that the periodic table still holds compounds awaiting discovery. In the group IV nitrides, only the IV_3N_4 materials are known, and nitrides containing Si(II) and Ge(II) may possibly be prepared by this combinatorial sputtering method. Possible uses for this material include optoelectronic energy conversion application such as light emitting diodes, tandem photovoltaics, and photoelectrochemical water splitting, though the structure must be solved and the defect density reduced before practical applications are realizable.

Chapter 5 is a brief report on antimony oxynitride, $Sb_3N_{5-2x}O_{3x}$, where $x \approx 0.4$. Antimony oxynitride is an amorphous material that possesses very low conductivity and exhibits optical properties suggesting a semiconducting electronic structure. The material is metastable, and decomposes in inert atmosphere near 400°C. Gradual transformation to crystalline Sb_2O_3 was observed at ambient conditions, and this affect was more pronounced at films grown at increased substrate temperatures.

Chapter 6 provides a summary of the conceptual insights contained in the preceding chapters. It also contains ideas to extend the work to future generations. The chapter is drolly subtitled "Great ideas undimmed by the challenges of actually trying them" and includes ideas to solve the crystal structure of $SnN_{1-\delta}$, ideas to prove that Cu_3N (or any material) has defect tolerant surfaces, and extendable work in the Cu-Sn-N system. The chapter also contains references and names of collaborators to assist future researchers in completing these ideas.

References

(1) Krupp, F.; Horn, M. *Earth: The Sequel the Race to Reinvent Energy and Stop Global Warming*; W.W. Norton & Company, Inc: New York, 2008.

(2) Yergin, D. *The Quest: Energy, Security, and the Remaking of the Modern World*; Penguin Books: London, 2011.

(3) Marchand, R.; Tessier, F.; Le Sauze, A.; Diot, N. Typical Features of Nitrogen in Nitride-Type Compounds. *Int. J. Inorg. Mater.* **2001**, *3*, 1143–1146.

(4) Akasaki, I. Nitride Semiconductors--Impact on the Future World. *J. Cryst. Growth* **2002**, *237-239*, 905–911.

(5) Chen, J.; Takanabe, K.; Ohnishi, R.; Lu, D.; Okada, S.; Hatasawa, H.; Morioka, H.; Antonietti, M.; Kubota, J.; Domen, K. Nano-Sized TiN on Carbon Black as an Efficient Electrocatalyst for the Oxygen Reduction Reaction Prepared Using an Mpg-C3N4 Template. *Chem. Commun.* **2010**, *46*, 7492–7494.

(6) CSG Titanium Nitride (TiN) Coatings http://coatingservicesgroup.com/titanium-nitride?gclid=CLapm46p8r4CFaNhMgodrjUA1Q (accessed Jun 11, 2014).

(7) Strite, S.; Lin, M. E.; Morkoc, H. Progress and Prospects for GaN and the III-V Nitride Semiconductors. *Thin Solid Films* **1993**, *231*, 197–210.

(8) Zakutayev, A.; Caskey, C. M.; Fioretti, A. N.; Ginley, D. S.; Vidal, J.; Stevanović, V.; Tea, E.; Lany, S. Defect Tolerant Semiconductors for Solar Energy Conversion. *J. Phys. Chem. Lett.* **2014**, *In press*.

(9) Ma, Y.; Oleynikov, P.; Li, Y.; Zhang, L.; Torres-pardo, A.; Gonza, J. M.; Terasaki, O.; Asahina, S.; Shima, M.; Cha, D.; *et al.* Cobalt Phosphate-Modified Barium-Doped Tantalum Nitride Nanorod Photoanode with 1.5% Solar Energy Conversion Efficiency. **2013**, 1–2.

(10) Boyko, T. D.; Hunt, A.; Zerr, A.; Moewes, A. Electronic Structure of Spinel-Type Nitride Compounds Si3N4, Ge3N4, and Sn3N4 with Tunable Band Gaps: Application to Light Emitting Diodes. *Phys. Rev. Lett.* **2013**, *111*, 097402.

(11) Perkins, J.; Paudel, T.; Zakutayev, a.; Ndione, P.; Parilla, P.; Young, D.; Lany, S.; Ginley, D.; Zunger, a.; Perry, N.; *et al.* Inverse Design Approach to Hole Doping in Ternary Oxides: Enhancing P-Type Conductivity in Cobalt Oxide Spinels. *Phys. Rev. B* **2011**, *84*, 1–8.

(12) Zakutayev, A.; Paudel, T. R.; Ndione, P. F.; Perkins, J. D.; Lany, S.; Zunger, A.; Ginley, D. S. Cation off-Stoichiometry Leads to High P-Type Conductivity and Enhanced Transparency in Co2ZnO4 and Co2NiO4 Thin Films. *Phys. Rev. B* **2012**, *85*, 085204.

(13) Zakutayev, A.; Zhang, X.; Nagaraja, A.; Yu, L.; Lany, S.; Mason, T. O.; Ginley, D. S.; Zunger, A. Theoretical Prediction and Experimental Realization of New Stable Inorganic Materials Using the Inverse Design Approach. *J. Am. Chem. Soc.* **2013**, *135*, 10048–10054.

CHAPTER 2 THIN FILM SYNTHESIS AND PROPERTIES OF COPPER NITRIDE, A METASTABLE SEMICONDUCTOR

Christopher M. Caskey,[a,b] Ryan M. Richards,[b] David S. Ginley,[a] and Andriy Zakutayev[a]

[a] National Renewable Energy Laboratory, Golden, Colorado, United States of America.
[b] Department of Chemistry and Geochemistry, Colorado School of Mines, Golden, Colorado, United States of America.

This paper is published in *Materials Horizon*s, a Royal Society of Chemistry journal. The first author was responsible for the synthesis, metrology, and analysis of results, as well as the writing of the manuscript. Reproduced by permission of the Royal Society of Chemistry. Article location: pubs.rsc.org/en/content/articlelanding/2014/mh/c4mh00049#!divAbstract

Abstract

Copper nitride (Cu_3N) thin films were grown by reactive sputtering using a high-throughput combinatorial approach with orthogonal gradients of substrate temperature and target-substrate distance. This technique enables high-throughput modulation of the anion activity, and is broadly applicable to the combinatorial synthesis of other materials. Stable, phase pure Cu_3N thin films were grown on glass substrates at temperatures between 150 and 200°C, depending on the target-substrate distance. These 00L oriented thin films have 10^{-3} S/cm conductivity and 1.5 eV optical absorption onset, making Cu_3N interesting for future studies in the context of solar energy conversion applications. The analysis of the synthetic results provides insights into the thermodynamic origins of the growth of metastable Cu_3N, and sets a nitrogen chemical potential of +1 eV/atom as a lower limit of the anion activity that can be achieved in non-equilibrium thin film growth of metastable materials. The first step towards testing the transferability of this result to other materials was made by reactive sputtering of tin, antimony, and bismuth in nitrogen.

Conceptual insights

This work evaluates the potential for energy conversion applications of copper nitride, a rather unexplored simple binary metastable nitride semiconductor. Studying copper nitride in the context of solar energy conversion applications provides a conceptual advance in the field of

optoelectronic nitride semiconductors, a field that so far has been limited to group III nitrides. Further, shown herein is a high-throughput method for varying the activity of the anion during sputtering. The high-throughput variation of nitrogen activity demonstrated in this paper represents a readily applicable advance in the field of combinatorial materials science, which to date primarily focused on varying cation composition. Finally, this work provides a framework for evaluating the likelihood of synthesizing other non- equilibrium materials. The rationalization of the thermodynamic metastability of the copper nitride material in terms of its convex hull and atomic nitrogen chemical potential is a conceptual insight in the field of materials-by-design, in particular computational materials prediction, and was extended to the nitrides of tin, antimony, and bismuth.

Introduction

Semiconducting materials play an important role in modern technology due to their broad use in integrated circuits, chemical sensors, photodetectors, and other technologies. Of particular importance are the optoelectronic energy conversion applications of semiconductors, such as solar cells, light-emitting diodes, and phototelectrochemical devices. Thus the quest for new semiconducting materials, particularly Earth-abundant non-toxic systems, is a major research thrust in the field of materials science. Copper nitride (Cu_3N) is a non-toxic metastable semiconducting material composed of Earth-abundant elements that has been proposed for applications in metallization layers,[1–3] tunnel junctions,[4] and resistive random-access memory (RRAM).[5] Stoichiometric, nitrogen-rich, and copper-rich Cu_3N materials have been previously reported.[6–9] The published electrical conductivities vary from ~30 S/cm [10] to ~10^{-3} S/cm [11] and the published optical absorption onsets are in the range of 1.4 to 1.8 eV.[7,11] There is disagreement regarding the value of the electronic band gap in Cu_3N, some of which may be the result of inconsistent terminology,[12] but reported values range from 0.25 eV to 1.90 eV.[7,13] This range nevertheless suggests that the binary Cu_3N has a potential as a solar absorber, and one of the goals of this work is to evaluate this possibility. The related ternary copper nitride $CuTaN_2$, which has the same linear N-Cu-N structural motifs as Cu_3N, has been recently reported to be promising for solar energy conversion applications because of its calculated band gap of 1.3 eV, measured absorption onset at 1.5 eV, and large calculated absorption coefficient of 10^5 cm^{-1} just 0.1 eV above the onset.[14] The N-Cu-N structural motifs in both Cu_3N and $CuTaN_2$ lead to anti-

bonding character of the valence band maximum, which could result in tolerance of the electrical properties of these copper nitride materials to structural defects.[15]

Most of the prior work on Cu_3N has been in thin film form with the samples produced by reactive sputtering. In the reactive sputtering of Cu_3N, nitrogen gas reacts with a copper metal target forming on its surface a copper nitride compound layer. Argon and nitrogen ions are created in plasma and accelerated by electric field towards the Cu target, sputtering off the Cu_3N compound layer. The sputtered Cu and N species, partially reacting in the gas phase, are collected on a glass substrate where the Cu_3N compound re-forms. Since Cu_3N is thermodynamically metastable with respect to decomposition into copper and nitrogen (+0.2 eV/at),[16] an important variable in the growth of Cu_3N is the activity of nitrogen at the film surface. For a given partial pressure of nitrogen, nitrogen activity is expected to decrease with increasing target-substrate distance due to gas-phase recombination of sputtered N species, and to decrease with increasing substrate temperature due to N_2 emission from the growing film. While the temperature[10,11,13,17] and pressure[6–8,11,17–19] variables of Cu_3N growth have been investigated, the target-substrate distance effect on nitrogen activity has not been studied so far. In this work we study the effect of nitrogen activity on the synthesis, structure and properties of copper nitride by simultaneous control of the target-substrate distance and substrate temperature.

An efficient way to establish fundamental synthesis-structure-property relationships in materials is the thin film combinatorial approach.[20] Our current implementation[21] of this high-throughput experimental strategy relies on (a) establishing gradients in growth parameters across the substrate during synthesis, (b) measuring the properties of the resulting combinatorial libraries as a function of position, and (c) analysing the resulting large amounts of data in a semi-automated way. Current combinatorial literature contains many examples of cation composition gradients,[22–26] and a few examples of substrate temperature gradients,[27–31] however, anion activity so far has not been studied via a high-throughput method. The present work fills this gap by growing copper nitride thin films with orthogonal gradients of temperature (T_S) and target-substrate distance (d_{TS}), such that each point on the substrate experiences a unique combination of T_S and d_{TS} growth conditions. In this experiment, equivalent nitrogen activity is achievable by different combinations of T_S and d_{TS}, enabling direct mapping of the constant nitrogen activity contours as a function of these two variables.

Experimental

The copper nitride thin film sample libraries were deposited on glass substrates by radio-frequency (RF) reactive sputtering of copper in 10 mTorr of nitrogen supplied through an RF atom source, balanced by 10 mTorr of argon supplied through a mass flow controller. The substrate was mounted at 45° relative to the sputter gun, resulting in a d_{TS} gradient of 13 to 15 cm. Only one side of the substrate was in thermal contact with a heater resulting in a T_S gradient of 140 - 280°C perpendicular to the d_{TS} gradient. Each sample library was characterized at 88 points for phase purity using X-ray diffraction (XRD), for absorption properties using optical spectroscopy and for conductivity using sheet resistance measured by four-point probe combined with thickness measured by X-ray fluorescence (XRF). The morphology of selected sample areas was imaged with scanning electron microscopy (SEM). More details about the experimental methods can be found in the supplementary information as well as our prior publications.[23,25]

Results and discussion

As shown in Figure 1, phase pure 00L oriented Cu_3N thin films were produced at low substrate temperatures and short target-substrate distances. Higher synthesis temperatures and longer target-substrate distances resulted in randomly oriented Cu_3N films, possibly seeded by nanoscale copper inclusions that are not detectable by XRD. The transition between the 00L oriented and the polycrystalline regions occurred between $T_S \approx 200$°C at d_{TS} = 13 cm and $T_S \approx$ 140°C at d_{TS} = 15 cm. Crystalline copper inclusions and subsequently pure copper films were observed in the XRD at the highest temperatures and the longest target-substrate distances. Note that the co-existence of Cu and Cu_3N indicates non-equilibrium synthesis according to the Gibbs phase rule. The production of both Cu^{1+} and Cu^0 species in this experiment demonstrates that the anion activity was modulated by the simultaneous control of the substrate temperature and the target-substrate distance. This strategy may be also applicable to other material systems, as shown later in the paper for tin, antimony and bismuth.

There are two likely mechanisms that can explain the measured synthesis phase map of the metastable copper nitride (Fig. 1). The first mechanism, which is thermodynamic in nature, is that a sufficiently high concentration of reactive nitrogen species is present at the surface of the growing copper nitride film at low target-substrate distances (due to decreased opportunity for

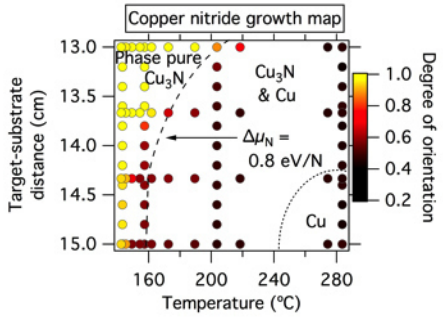

Fig. 2.1: Copper nitride growth map as a function of substrate temperature and target-substrate distance. The dashed line separates growth conditions which produced phase pure Cu_3N from those which produced Cu_3N & Cu. Along this line $\Delta\mu_N$= +0.8 eV/N. The dotted line separates growth conditions which produced Cu_3N & Cu from those which produced Cu. The colour scale is the degree of crystallographic orientation and is the sum of the areas of the 001 and 002 peaks divided by the areas of the four measured Cu_3N peaks, with the value of 0.3 corresponding to a randomly oriented film.

$2N/N_2$ gas phase neutralization) and low substrate temperatures (due to less likely reemission of N_2 from the growing film). The second mechanism, kinetic in origin, is that the high arrival rates of copper and nitrogen atoms suppress the reemission of N_2 by adding more material before molecular nitrogen can form. In order to test these two hypotheses, we compared the films grown with (i) the nitrogen atom source on (250 W) and off (0 W) and thus resulting in different concentrations of reactive nitrogen species, and (ii) with different power applied to Cu target (15 W, 20 W and 25 W) and thus resulting in different rates of arriving copper and nitrogen atoms. As shown in supplementary Figure S1, the first experiment led to dramatic decrease in the size of the phase pure region while the second experiment did not significantly change the results when compared to Fig. 1. The results of these two experiments indicate that in the studied range of conditions the concentration of reactive nitrogen species rather than the rate of arrival of copper and nitrogen atoms controls the growth chemistry of copper nitride. Thus, sparingly, the driving force behind the synthesis of phase-pure metastable Cu_3N can be viewed as thermodynamic rather than kinetic in its origin.

As show in Figure 2, conductivities of the 00L oriented thin films deposited at <160°C were consistently in the range of $5x10^{-4}$ S/cm to $2x10^{-3}$ S/cm. The conductivity numbers and XRD patterns of these Cu_3N samples did not change after 1+ years of sample storage at ambient conditions, suggesting that the films are shelf-stable. By increasing the substrate temperature to 170 - 220°C, the conductivity rose by a factor of 10 - 1000, and for some of these samples copper inclusions were observed in the XRD (Fig. 2 right axis). Such inclusions or similar copper richness are possible reasons for large variations of copper nitride conductivity reported

in the literature.[7,32] Thin films deposited at 270 - 280°C substrate temperature had 10^3 S/cm conductivity consistent with predominantly metallic copper clearly observed by XRD.

As demonstrated in Figure 3, for the phase pure 00L oriented Cu_3N thin films grown at a substrate temperature of 160°C and at short (13.0 - 13.5 cm) target-substrate distances, the optical absorption onset ranged from 1.4 to 1.6 eV and the onset was steepest (lower portion of

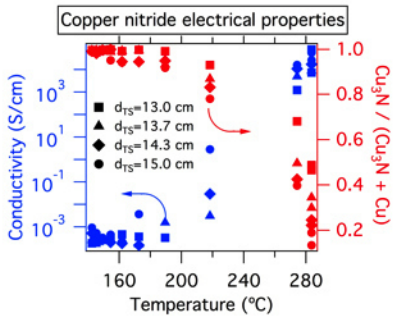

Fig. 2.2: Electrical properties and phase purity of copper nitride thin films. The right axis is the area of Cu_3N XRD peaks divided by the areas of Cu_3N and Cu XRD peaks. Thus a value of unity corresponds to phase pure Cu_3N. The spread of data for fixed T_S results from the differences in d_{TS} = 13.0, 13.7, 14.3 and 15.0 cm.

Fig. 3a and Fig. 3b). In contrast, significant sub-gap absorption was observed in the polycrystalline samples grown at longer target-substrate distances with a decrease in the steepness of the onset (dashed line in Fig. 3a and Fig. 3b). Finally, small copper inclusions are observed in XRD at the longest target-substrate distances. At d_{TS} = 15 cm, the sub-gap absorption increases significantly, presumably due to increased concentration of these metallic inclusions (upper trace in Fig. 3a and 3b). We note that Fig. 3a is very similar to the results obtained by Pierson when the flow rate and partial pressure of nitrogen was modulated:[6] the present target-substrate distance gradient appears to mimic changes in partial pressure of nitrogen.

Synthesis of 00L oriented copper nitride thin films with low conductivity and no sub-gap absorption satisfies the minimal requirements for this material to be studied in the future as a solar absorber. However, optical absorption and electrical conductivity are not the only important parameters for this and other semiconductor applications. For example in photovoltaics, the minority carrier lifetime, which is determined by defect density (reflected by the measured sub-gap absorption), as well as the concentration and mobility of the majority charge carriers (on which the measured electrical conductivity depends), are crucial parameters for device performance and would need to be studied. We also note that the measured absorption onset

(which defines the short circuit current limit of a solar cell) does not necessarily correspond to the band gap (which sets the limit of the open-circuit voltage of a photovoltaic device), particularly for semiconductors that have an electronic structure with indirect or forbidden character of the band gap. Finally, the long-term operational performance of a metastable semiconductor like Cu_3N would be necessary to consider. Future work will focus in more detail on the stability, transport, optical, and electronic structure properties of copper nitride with the goal to assess more rigorously its potential as a solar energy conversion material.

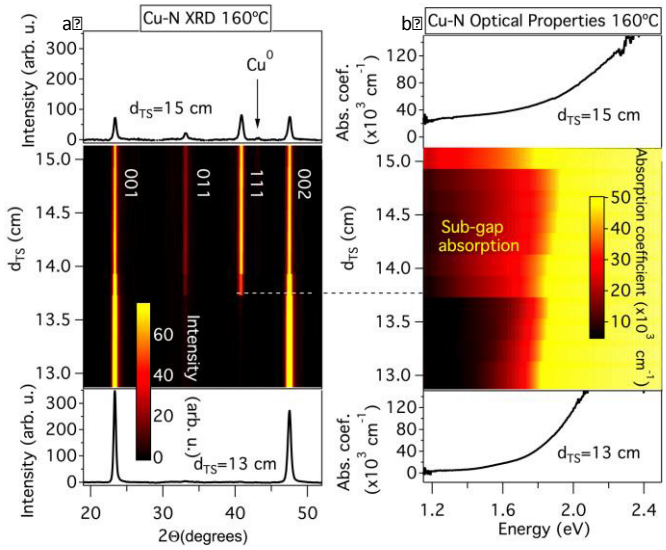

Fig. 2.3: Structural and optical properties of Cu_3N thin films: (a) XRD patterns and (b) optical absorption spectra at different target-substrate distances (d_{TS}) and a constant substrate temperature of 160°C. An alternative form of this figure is available in the supplementary information Figure S2.

It is interesting to note that not only the phase purity and preferential orientation, but also the grain size of the copper nitride thin films depend on both substrate temperature and target-substrate distance. From the microscopy measurements shown in Figure 4, films with small grains (30 to 50 nm) were observed in the 00L oriented regions at the lowest temperature and shortest target-substrate distance (Fig. 4a). Polycrystalline Cu_3N films with grains of 50-100 nm (Fig. 4c) were grown at higher temperatures and longer target-substrate distances. A narrow band of 200 nm crystallites (Fig. 4c), visible to the eye as a dark stripe across the sample (Fig. 4 top left), was observed near the transition from textured to polycrystalline film. These 200 nm grains decreased in concentration with increasing distance from the transition region (Fig. 4 centre). The largest grains were 300 nm in size and were grown at a temperature of 230°C, where copper

inclusions were observed by XRD. Above this temperature the copper nitride decomposed, and the remaining copper was composed of complex, voided crystallites 100 to 200 nm in size. Cross-sections of the thin film regions with the 00L-textured (Fig. 4a) and polycrystalline (Fig. 4c) phase pure Cu_3N revealed columnar structures while larger grains were observed in the transition region between these two limiting cases (Fig. 4b). While the mechanistic details of growth are not known, we propose that changes in anion activity leading to changes in energy, charge and composition of the grain surfaces are likely responsible for the observed variations in morphology. Specifically, we hypothesize that nitrogen-rich grain surfaces repel each other leading to small 00L oriented grains (Fig. 4a), copper-rich grain surfaces coalesce but seed small polycrystalline grains (Fig. 4c), and stoichiometric grain surfaces coalesce forming the largest grains in the narrow region between these cases (Fig. 4b). The elemental composition of the grains at the microstructure level is currently unknown. It is interesting that small changes in target-substrate distance and temperature have such dramatic affects on film morphology, and further tuning of these parameters could lead to intentional control of film roughness.

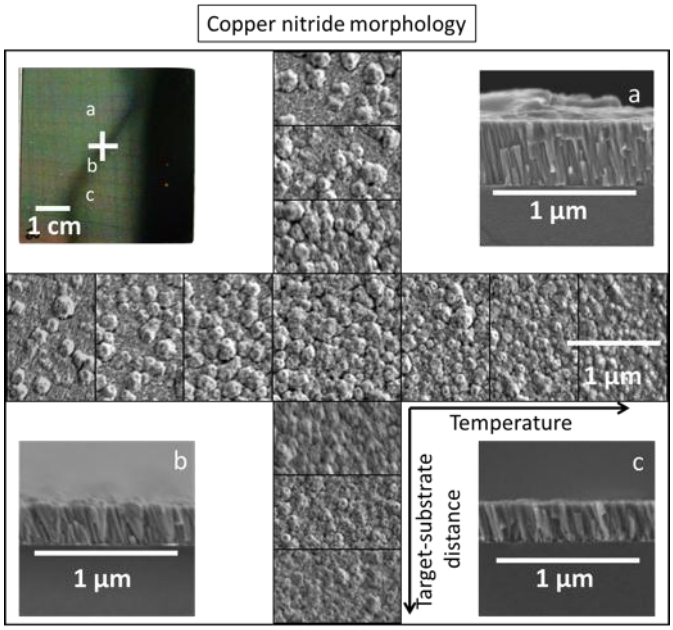

Fig. 2.4: Morphological properties of the Cu_3N thin films. Top left: Photograph of a combinatorial thin film sample with the cross denoting the locations of SEM surface images (centre) and letters indicating locations of cross-sections. Centre: SEM surface images of copper nitride thin films taken 1 mm apart along the cross shown in the photograph. The cross-sectional images of the film are shown for the (a) 00L textured, (b) transition, and (c) polycrystalline regions of the film.

The ability to synthesize phase pure Cu_3N thin films with 00L orientation (Fig. 1), semiconducting properties (Fig. 2 and Fig. 3) and reasonable morphology (Fig. 4), despite the thermodynamically metastable character of this material may be attributed to the high energy of copper and nitrogen precursors used in the non-equilibrium sputtering process. In thermodynamic equilibrium, Cu_3N is unstable (ΔH^{ST}_{Cu3N} = +0.2 eV/atom) with respect to decomposition into metallic copper solid and molecular nitrogen gas standard reference states:[16]

$$3\ Cu\ (metallic) + \tfrac{1}{2}\ N_2 \rightarrow Cu_3N\ (+0.2\ eV/atom) \qquad (1)$$

In contrast, Cu_3N is stable (ΔH^{AT}_{Cu3N} = -3.6 eV/atom) with respect to decomposition into the copper atoms (+3.5 eV/at with respect to copper solid) and nitrogen atoms (+4.9 eV/atom with respect to molecular nitrogen[33]) that are used as precursors in the non-equilibrium sputtering process:[34]

$$3\ Cu\ (atoms) + N \rightarrow Cu_3N\ (-3.6\ eV/atom) \qquad (2)$$

This difference can be visualized by the energy vs. composition diagram of the copper-nitrogen system shown in Figure 5. It is notable that the Cu-N ground state line forms a "convex hull"[35] with Cu_3N at the bottom when referenced to copper atoms and nitrogen atoms, in contrast to the case of Cu solid and N_2 gas. This illustrates why it is possible to make metastable Cu_3N from sputtered copper atoms and nitrogen atoms despite the positive formation enthalpy of this material with respect to the standard states.

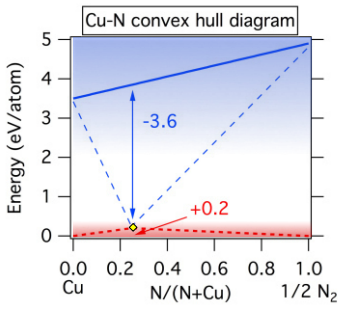

Fig. 2.5: Convex hull diagram for Cu-N system with respect to atomic copper and atomic nitrogen (blue lines) as well as molecular nitrogen and solid copper standard reference states (red lines).

It is possible to use the ΔH^{AT}_{Cu3N} = -3.6 eV/atom formation enthalpy of Cu_3N obtained from the quasi-equilibrium analysis (Eq. 1 and Eq. 2) and visualized in Fig. 5 to quantify the effective partial pressure of nitrogen atoms as well as the nitrogen chemical potential as a function of target-substrate distance during the Cu_3N growth. The enthalpy of formation of Cu_3N is equal to the sum of the chemical potentials of atomic copper ($\Delta\mu_{Cu}$) and atomic nitrogen ($\Delta\mu_N$) as described by:

$$\Delta H^{AT}_{Cu3N} = \Delta\mu_N + \Delta\mu_{Cu} = \text{-3.6 eV/atom} \qquad (3)$$

In quasi-equilibrium with copper atoms (indicated by the dashed line in Fig. 1) $\Delta\mu_{Cu} = 0$ eV/atom and thus from Eq. 3 the chemical potential of nitrogen is $\Delta\mu_N$ = -3.6 eV/atom. This $\Delta\mu_N$ can be written using as:[36]

$$\Delta\mu_N(T,P) = \Delta\mu^o_N(T,P^\circ) + k_B T * ln(P/P^\circ) \qquad (4)$$

where T is the temperature, P is the pressure, P° is the reference pressure, k_B is the Boltzman constant and $\Delta\mu_N^\circ(T,P^\circ)$ is the temperature-dependent standard free energy calculated using the Shomate equation and coefficients from the NIST-JANAF thermochemical tables.[37]

To determine the range of atomic nitrogen partial pressures, one can solve equations (3) and (4) knowing from Fig. 1 the temperatures at which Cu_3N is in equilibrium with Cu. We find that the pressure varies between 10^{-31} Torr and 10^{-26} Torr as the target-substrate distance changes from 13 cm to 15 cm and the equilibrium temperature varies from 150 to 200°C. Such remarkably small partial pressures of atomic nitrogen required to synthesize copper nitride is the result of large cohesive energy of copper solid and nitrogen molecules (Fig. 5). We note that our effective partial pressure of atomic nitrogen corresponds to the net chemical potential of all nitrogen species present in the discharge.[38,39] To assess the highest achievable effective chemical potential of nitrogen for this synthetic technique, we substitute the highest pressure value calculated above (10^{-26} Torr) and a reasonable expected temperature for a substrate without active heating or cooling (100°C) back into Eq. 4, producing a value of -2.8 eV/N. This is 2.8 eV/N below the atomic Cu to atomic N tie line, and 1 eV/N *above* the solid Cu to molecular N_2

tie line (Fig. 5). This indicates that metastable binary nitrides that require nitrogen chemical potential of up to +1 eV/atom could potentially be synthesized using reactive sputtering with an atomic nitrogen source. While this limit is likely to be specific for the deposition instrument used in this experiment, the chemical potential limit of any other instrument may be evaluated by finding the maximum temperature at which a known metastable material can be synthesized phase-pure and then following the analysis presented above.

The quasi-thermodynamic analysis presented above provides some insight into the range of the chemical potentials that are achievable by non-equilibrium growth techniques. This insight is important for the computational design of new materials, which has recently attracted significant attention[40,41] and has resulted in a few experimental discoveries of previously unreported compounds.[42,43] However, a large fraction of materials that are currently being synthesized are thermodynamically unstable.[44] Also, it has been recently noted[45] that a large number of theoretically predicted useful ternary materials are unstable with respect to competing phases. Referencing these hypothetical non-equilibrium materials to their atomic components, as illustrated in Fig. 5, can be used to evaluate which of them have any chance of being synthetically achievable. Specifically, as illustrated above for the binary metal nitrides it can be expected that metastable materials that require up to +1 eV/atom nitrogen chemical potential should be synthesizable. However, it is important to emphasize that such analysis would provide a *necessary but not sufficient* metric of synthesizability, because a sufficiently high kinetic barrier to decomposition must also exist to stabilize the non-equilibrium phase. This is likely to be especially important in the case of ternary or more chemically complex compounds where disproportionation into constituent binaries is at least as important as decomposition into elemental phases.

As a first step towards demonstrating the generalizability and predictability of the quasi-thermodynamic analysis for other nitride systems, we selected three metal nitrides (tin nitride, antimony nitride and bismuth nitride) and attempted their synthesis. Tin nitride, Sn_3N_4, can be used to show the generalizability of our quasi-thermodynamic model. Using the fitted elemental reference energies approach (FERE)[46] Sn_3N_4 has an formation enthalpy of +1.56 eV/formula unit, or about +0.4 eV/N with respect to decomposition into Sn metal and N_2 gas. Using an analysis similar to Fig 5. (cohesive energy of tin = 3.1 eV/atom) we obtain a required atomic nitrogen chemical potential of -3.7 eV/N for synthesis of this material. At our maximum

calculated partial pressure of atomic nitrogen (10^{-26} Torr) and using Eq. 4 we estimate that Sn_3N_4 should be synthesizable up to 220°C. This is, as expected, higher than the maximum temperature for the less-stable Cu_3N, and should be a good test for the generality of the quasi-thermodynamic chemical potential model. The formation energies and the crystal structures of the two other nitrides, antimony nitride and bismuth nitride, have not been reported in literature, so the maximum temperature of their synthesis is a prediction of their stability relative to Cu_3N. The results of investigations of Sn-N, Sb-N and Bi-N are compared to Cu-N in Table 1 and in Figure S3 of the supplementary information.

The synthetic results indicate that tin nitride does not start decomposing into Sn and N_2 until higher temperatures than Cu_3N, qualitatively supporting the quasi-thermodynamic analysis. However the metallic Sn did not precipitate out of Sn_3N_4 until 450°C, which is above the 220°C estimated from the quasi-thermodynamic model. We attribute this difference to the multivalent character of tin(which can be not only in IV+ but also in II+ valence state), since other nitrogen-deficient tin nitride phases were observed at intermediate temperatures. More information about the structure and physical properties of these tin nitrides will be published in the future. Overall, the results for Sn-N are qualitatively consistent with the quasi-thermodynamic model suggesting its generalizability, but more quantitative work on this topic is needed.

Table 1: Chemical formula, crystal structure, heat of formation of metastable nitrides and the lowest temperature at which crystalline metallic species were observed in XRD at d_{TS}=13 cm.

Formula	Structure	ΔH_f (eV/N)	T_{met} (°C)
Sn_3N_4	spinel	0.4	450
Cu_3N	anti-ReO_3	0.8	200
Sb_xN_y	unknown	unknown	350
Bi_xN_y	unknown	unknown	ambient

Antimony nitride was observed as an amorphous semiconducting film up to 350°C, and metallic bismuth was the only crystalline phase obtained at ambient substrate temperature. These

results indicate that the thermodynamic stability of Sb-N is comparable to that of Sn-N, and that the stability of Bi-N is lower than that of Cu_3N. These qualitative predictions require further quantification and call for further experimental and theoretical verification, but they are consistent with the scarce literature on Sb-N and Bi-N materials. For antimony nitride, amorphous semiconducting Sb-N thin films[47] and material with an Sb:N = 3:1 composition[48] have been reported, suggesting it may have stability similar to Sn-N. In contrast, early reports on bismuth nitride suggest that it is quite reactivive,[49,50] and thus likely less thermodynamically stable than Cu_3N. More detailed results of the synthesis and stability of Sb-N and Bi-N will be the subject of future publications.

Overall, the results of the Sn-N studies compared to Cu_3N indicate that the quasi-thermodynamic analysis may be extendable to other metastable nitride materials, and a first attempt of prediction based on such extension is made for the Sb-N and Bi-N materials, but clearly further research in this area is needed. Once the atomic chemical potential model is fully established, it can be used for predictions of the thermochemistry related quantities that depend on chemical potential (such as defect formation energies and charge carrier concentrations) for both metastable and stable nitrides. If successful, such approach may also be generalizable to other anions such as O, F, or S in the future.

Conclusions

In summary, we report the synthesis and semiconducting properties of metastable copper nitride thin films prepared using reactive sputtering. Phase pure Cu_3N thin films were synthesized in the presence of a nitrogen atom source using a high-throughput combinatorial approach with orthogonal gradients of target-substrate distance and substrate temperature, both affecting the nitrogen activity. In turn, the nitrogen activity influences both the phase purity and the morphology of the resulting Cu_3N thin films. This high-throughput synthesis technique is a valuable contribution to combinatorial materials science, which up to date has focused primarily on cation gradients. The phase pure 00L oriented Cu_3N thin films have conductivities of 10^{-3} S/cm and a 1.4 – 1.6 eV optical absorption onset. These results indicate that Cu_3N may be a promising candidate for solar cell absorber applications, calling for more detailed studies on this topic. Additionally, we report the quasi-thermodynamic chemical potential model for the synthesis of Cu_3N, which explains the sputtering growth of this metastable material by

referencing it to its atomic (Cu and N) rather than standard (Cu solid and N_2 gas) reference states. Using this model, we estimate that at least +1 eV/atom effective nitrogen chemical potential is achievable in the process of reactive sputtering with a nitrogen atom source. This result, and the underlying quasi-thermodynamic model, may be generalizable to theoretical prediction and experimental synthesis of other metastable materials as exemplified for the nitrides of antimony, tin, and bismuth.

Acknowledgements

This research is supported by the U.S. Department of Energy, office of Energy Efficiency and Renewable Energy, as a part of the "Ternary Copper Nitride Absorbers" Next Generation PV II project within the SunShot initiative. The authors would like to thank John D. Perkins, Stephan Lany, Vladan Stevanović and Julien Vidal for illuminating discussions and Sn_3N_4 FERE calculations.

Notes

Electronic Supplementary Information (ESI) available: More detailed experimental methods and a comparison of films grown with and without the atomic nitrogen source and at different target powers is available. A reformatted version of Fig. 3 is presented. Additionally, XRD patterns from the investigations of tin, antimony, and bismuth systems are available. See DOI: 10.1039/c4mh00049h

Supplementary information

Copper nitride thin films were prepared by radio-frequency (RF) reactive magnetron sputtering of a 50 mm circular copper target in an argon and nitrogen atmosphere. Power supplied to the target was 15, 20, or 25 W, and the depositions were carried out with the target fully poisoned. A 50 mm by 50 mm glass substrate was cleaned in an ultrasonic bath, first with acetone and second with isopropanol. The substrate was then subjected to oxygen plasma to remove any organic residue. This substrate was mounted in the deposition chamber at an angle of 45° relative to the sputter gun. The near side of the sample was 13 cm from the gun and the far side of the sample was 15 cm from the gun. The top side of the

substrate was mounted with silver paste to a heater set to 250 °C, and the remainder of the substrate was suspended in vacuum. This produced a temperature gradient perpendicular to the target-substrate distance (d_{TS}) gradient, such that each point on the substrate experienced different growth conditions. The temperature at the substrate surface varied from 280 °C (slightly above the set point) to 140 °C. Prior to deposition, the target was preconditioned by sputtering for at least 30 minutes with a shutter in front of the substrate.

The flow rate of both nitrogen and argon was 10 sccm, and the total chamber pressure was 20 mTorr. The argon was supplied through a mass flow controller and the nitrogen was supplied through an atomic gas source (Oxford Applied Research model HD25) and controlled by a calibrated needle valve. The atomic gas source is designed to crack gas molecules using a radio-frequency field, and was turned on to produce some of the samples and kept off for others. When the atomic gas source was on, the power was set to 250 W. After a 3.5 hour deposition, the sample was allowed to cool with argon and nitrogen flowing and the sputter gun and atomic gas source off, and it was then removed from the chamber. As shown in Fig. S1a, using an atomic nitrogen source significantly improves the phase purity and preferential orientation of Cu_3N thin films. In contrast, changing the power applied to the copper target with the nitrogen atom source in operation does not appreciably influence the phase purity and 00L orientation of the resulting Cu_3N thin films, under otherwise equal deposition conditions (Fig. S1b). Together, these two results indicate that the high activity of nitrogen is a more important component for growth of phase-pure Cu_3N thin films than the rate at which these thin films are synthesized, within the range of investigated synthesis conditions.

Both structural and optical properties changed as a function of target-substrate distance. Shown in Figure S2 is an alternative representation of Figure 3 from the main text.

Analysis of our results from copper nitride indicate that binary nitride compounds with ΔH_f = +1eV/N should be accessible by the method of sputtering with an atomic nitrogen source. This motivated the synthetic study of three other metastable nitrides of tin, antimony and bismuth. Tin nitride adopts the spinel crystal structure and has Sn_3N_4 chemical composition. No crystallographic information or chemical composition is available in literature or databases for either bismuth nitride or antimony nitride. Shown in Figure S3 are XRD patterns of the results of sputtering these metals in a nitrogen and argon atmosphere.

The top trace in each pane is the lowest temperature at which metallic precipitates were observed in XRD at a target-substrate distance of 13 cm.

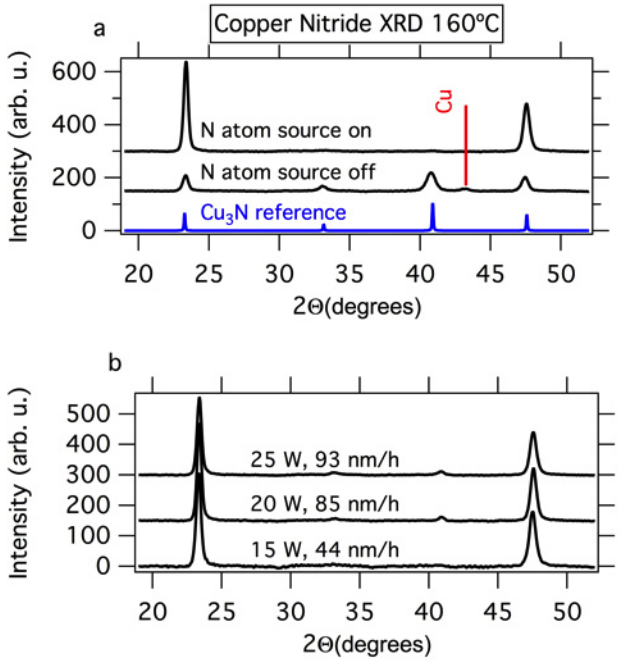

Fig. S2.1 (a) XRD patterns of films grown at 20 W Cu, 160 °C, and d_{TS} = 13 cm with the cracker on at 250 W (on) and 0 W (off). (b) XRD patterns of films grown at 160 °C, and d_{TS} = 13.8 cm with the cracker on at 250 W. All XRD patterns are normalized for film thickness and diffraction collection time.

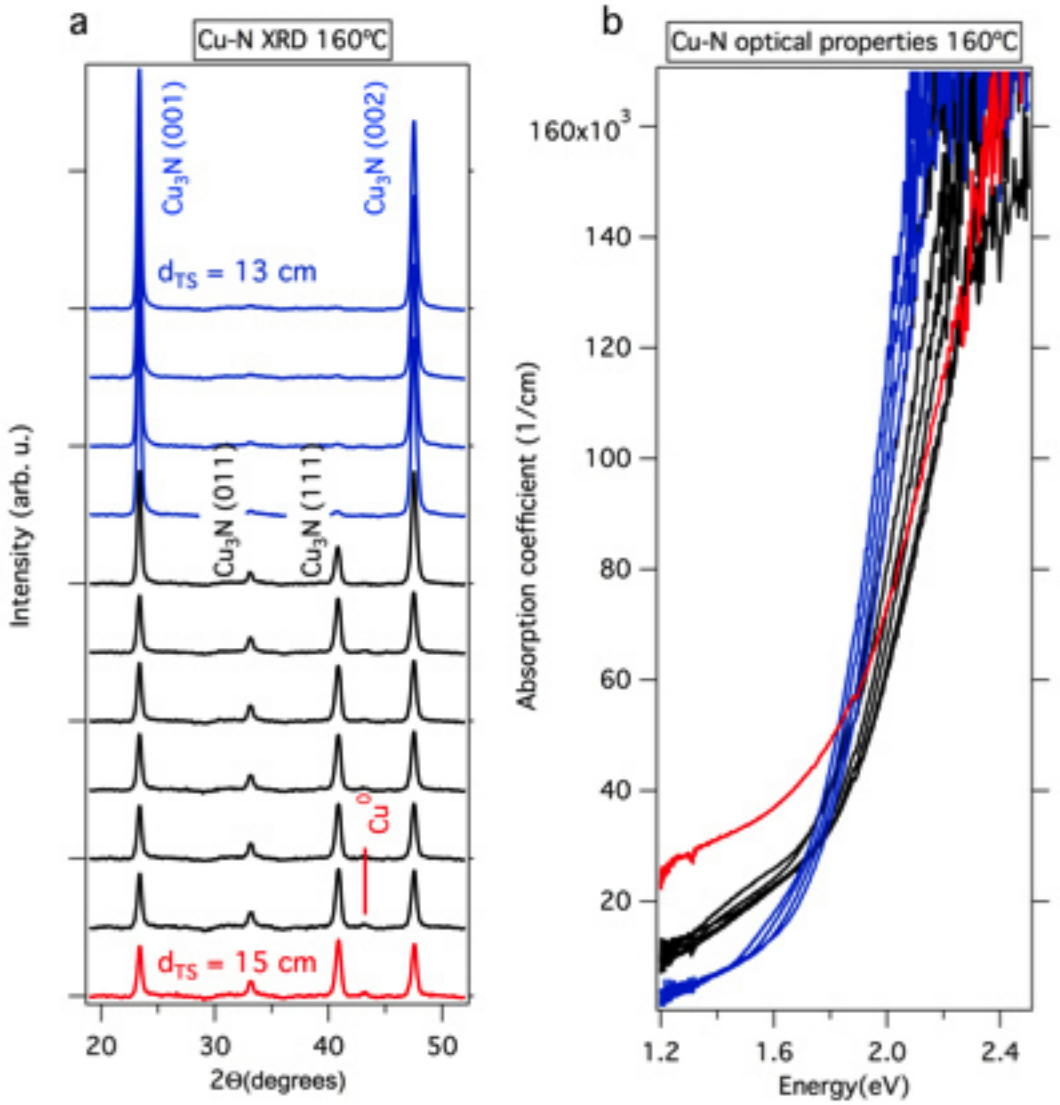

Fig. S2.1 (a) XRD patterns of films grown at 20 W Cu, 160 °C, and d_{TS} ranging from 13 cm (top blue trace) to 15 cm (red trace). (b) Optical characterization of the same films.

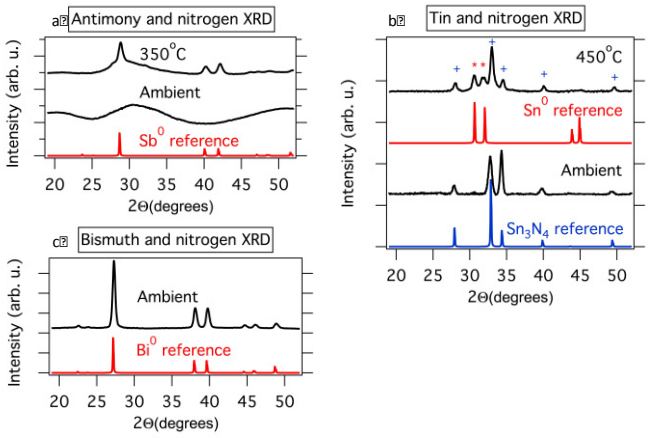

Fig. S3: XRD patterns of films obtained by sputtering (a) antimony, (b) tin, and (c) bismuth in a nitrogen and argon atmosphere with an atomic nitrogen source. In the top pattern of (b) metallic tin is marked by (*) while tin nitride is marked with (+).

References

1. L. Maya, *J. Vac. Sci. Technol. A*, 1993, **11**, 604–608.

2. T. Maruyama and T. Morishita, *Appl. Phys.*, 1996, **69**, 890–891.

3. R. Cremer, M. Witthaut, D. Neusch, C. Trappe, M. Laurenzis, O. Winker, and H. Kurz, *Mikrochim. Acta*, 2000, **133**, 299–302.

4. D. M. Borsa, S. Grachev, C. Presura, and D. O. Boerma, *Appl. Phys. Lett.*, 2002, **80**, 1823–1825.

5. W. Zhu, X. Zhang, X. Fu, Y. Zhou, S. Luo, X. Wu, I. Resistive, and T. Cu, *Phys. Status Solidi A*, 2012, 1–6.

6. J. F. Pierson, *Vacuum*, 2002, **66**, 59–64.

7. N. Gordillo, R. Gonzalez-Arrabal, M. S. Martin-Gonzalez, J. Olivares, A. Rivera, and F. Briones, *J. Cryst. Growth*, 2008, **310**, 4362–4367.

8. N. Gordillo, R. Gonzalez-Arrabal, P. Diaz-Chao, J. R. Ares, I. J. Ferrer, F. Yndurain, and F. Agulló-López, *Thin Solid Films*, 2013, **531**, 588–591.

9. A. L. Ã. Ji, R. Huang, Y. Du, C. R. Li, Y. Q. Wang, and Z. X. Cao, *J. Cryst. Growth*, 2006, **295**, 79–83.

10. T. Maruyama and T. Morishita, *J. Appled Phys.*, 1995, **78**, 1–5.

11. T. Nosaka, M. Yoshitake, A. Okamoto, and S. Ogawa, *Thin Solid Films*, 1999, **348**, 8–13.

12. J.-L. Bredas, *Mater. Horizons*, 2014, **1**, 17.

13. F. Hadian, a. Rahmati, H. Movla, and M. Khaksar, *Vacuum*, 2012, **86**, 1067–1072.

14. M. Yang, A. Zakutayev, J. Vidal, X. Zhang, D. S. Ginley, and F. J. DiSalvo, *Energy Environ. Sci.*, 2013, **6**, 2994.

15. A. Zakutayev, C. M. Caskey, A. N. Fioretti, D. S. Ginley, J. Vidal, V. Stevanović, E. Tea, and S. Lany, *J. Phys. Chem. Lett.*, 2014, **5**, 1117–1125

16. S. Lany, *Phys. Rev. B*, 2008, **78**, 245207.

17. Z. Q. Liu, W. J. Wang, T. M. Wang, S. Chao, and S. K. Zheng, *Thin Solid Films*, 1998, **325**, 55–59.

18. J. F. Pierson, D. Wiederkehr, and A. Billard, *Thin Solid Films*, 2005, **478**, 196–205.

19. G. H. Yue, P. X. Yan, and J. Wang, *J. Cryst. Growth*, 2005, **274**, 464–468.

20. M. L. Green, I. Takeuchi, and J. R. Hattrick-Simpers, *J. Appl. Phys.*, 2013, **113**, 231101.

21. A. Zakutayev, F. J. Luciano, V. P. Bollinger, A. K. Sigdel, P. F. Ndione, J. D. Perkins, J. J. Berry, P. a Parilla, and D. S. Ginley, *Rev. Sci. Instrum.*, 2013, **84**, 053905.

22. I. Takeuchi, R. B. van Dover, and H. Koinuma, *MRS Bull.*, 2002, 301–308.

23. A. Zakutayev, T. R. Paudel, P. F. Ndione, J. D. Perkins, S. Lany, A. Zunger, and D. S. Ginley, *Phys. Rev. B*, 2012, **85**, 085204.

24. H. Koinuma and I. Takeuchi, *Nat. Mater.*, 2004, **3**, 429–38.

25. A. Zakutayev, J. D. Perkins, P. A. Parilla, N. E. Widjonarko, A. K. Sigdel, J. J. Berry, and D. S. Ginley, *MRS Commun.*, 2011, **1**, 23–26.

26. V. Cloet, A. Raw, K. R. Poeppelmeier, G. Trimarchi, H. Peng, J. Im, A. J. Freeman, N. H. Perry, T. O. Mason, A. Zakutayev, P. F. Ndione, D. S. Ginley, and J. D. Perkins, *Chem. Mater.*, 2012, **24**, 3346–3354.

27. T. Chikyow, P. Ahmet, K. Nakajima, T. Koida, M. Takakura, M. Yoshimoto, and H. Koinuma, *Appl. Surf. Sci.*, 2002, **189**, 284–291.

28. A. Zakutayev, N. H. Perry, T. O. Mason, D. S. Ginley, and S. Lany, *Appl. Phys. Lett.*, 2013, **103**.

29. T. Koida, D. Komiyama, H. Koinuma, M. Ohtani, M. Lippmaa, and M. Kawasaki, *Appl. Phys. Lett.*, 2002, **80**, 565.

30. A. Submaraniyan, J. D. Perkins, R. P. O'Hayre, S. Lany, V. Stephanovic, D. S. Ginley, and A. Zakutayev, *APL Mater.*, 2014, **2**.

31. S. Ohashi, M. Lippmaa, N. Nakagawa, H. Nagasawa, H. Koinuma, and M. Kawasaki, *Rev. Sci. Instrum.*, 1999, **70**, 178.

32. Y. Du, A. L. Ã. Ji, L. B. Ma, Y. Q. Wang, and Z. X. Cao, *J. Cryst. Growth*, 2005, **280**, 490–494.

33. B. deB Darwent, 1970.

34. I. Petrov, A. Myers, J. E. Greene, and J. R. Abelson, *J. Vac. Sci. Technol. A*, 2012, **2846**, 2846–2854.

35. S. Wei, L. Ferreira, and a Zunger, *Phys. Rev. B. Condens. Matter*, 1990, **41**, 8240–8269.

36. K. Reuter and M. Scheffler, *Phys. Rev. B*, 2001, **65**, 1–11.

37. M. W. J. Chase, *NIST Web B.*, 1998.

38. A. J. Ptak, K. S. Ziemer, M. R. Millecchia, C. D. Stinespring, and T. H. Myers, *MRS Internet J. Nitride Semicond.*, 1999, **4S1**, 1–6.

39. W. E. Hoke, P. J. Lemonias, and D. G. Weir, *J. Cryst. Growth*, 1991, **111**, 1024–1028.

40. B. Meredig and C. Wolverton, *Nat. Mater.*, 2013, **12**, 123–7.

41. S. Curtarolo, G. L. W. Hart, M. B. Nardelli, N. Mingo, S. Sanvito, and O. Levy, *Nat. Mater.*, 2013, **12**, 191–201.

42. A. Zakutayev, X. Zhang, A. Nagaraja, L. Yu, S. Lany, T. O. Mason, D. S. Ginley, and A. Zunger, *J. Am. Chem. Soc.*, 2013, **135**, 10048–54.

43. G. Hautier, A. Jain, and S. P. Ong, *J. Mater. Sci.*, 2012, **47**, 7317–7340.

44. J. E. Saal, S. Kirklin, M. Aykol, B. Meredig, and C. Wolverton, *Jom*, 2013, **65**, 1501–1509.

45. X. Zhang, L. Yu, A. Zakutayev, and A. Zunger, *Adv. Funct. Mater.*, 2012, **22**, 1425–1435.

46. V. Stevanović, S. Lany, X. Zhang, and A. Zunger, *Phys. Rev. B*, 2012, **85**, 115104.

47. T. Shiraishi, A. Yasuyuki, and S. Yamazaki, *J. Non. Cryst. Solids*, 1985, **77& 78**, 1313–1316.

48. Q. Sun, W.-J. Li, and Z.-W. Fu, *Solid State Sci.*, 2010, **12**, 397–403.

49. I. Schrman and W. C. Fernelius, *J. Am. Chem. Soc.*, 1930, **52**, 2425–2430.

50. E. C. Franklin, *J. Am. Chem. Soc.*, 1905, **836**, 820–851.

CHAPTER 2 SEMICONDUCTING PROPERTIES OF SPINEL TIN NITRIDE AND OTHER IV_3N_4 POLYMORPHS

Christopher M. Caskey,[1,2] Jason A. Seabold,[1] Vladan Stevanović,[1,2] Ming Ma,[3] Wilson A. Smith,[3] David S. Ginley,[1] Nathan R. Neale,[1] Ryan M. Richards,[1,2] Stephan Lany,[1] Andriy Zakutayev[1]

1) National Renewable Energy Laboratory
2) Colorado School of Mines
3) Delft Technical University

This manuscript will be submitted to a peer-reviewed journal for publication. The first author was responsible for thin-film synthesis, solid-state characterization, and manuscript preparation.

Abstract

Tin nitride, Sn_3N_4, is a semiconductor composed of abundant elements with a band gap in the visible range making it an excellent candidate for optical and electronic applications. In this work, the semiconducting properties of tin nitride are explored by thin-film experiments and first-principles theory to evaluate the efficacy of this material for optoelectronic technologies. A computational study of related group IV nitride polymorphs provides additional insight into the properties and challenges associated with this class of semiconductors. From theory for tin nitride, we determined a band gap of 1.54 eV, and predict a large hole effective mass and a small electron effective mass. Experimentally, the carrier concentration was found to be as low as 10^{18} cm^{-3} (n-type), with an electron mobility of ~1 cm^2/Vs, a minority carrier diffusion length of 50-100 nm, and an ionization potential of 5.9-6.0 eV. Periodic and structural trends in electrical properties are observed in the IV_3N_4 polymorphs: Hole effective masses generally increase down the period and are structure-dependent while electron effective masses decrease down the period and show no strong structural trends. The results provide insight into the solid-state chemistry of the materials family and suggest that changing composition in the group IV nitride alloys will have a large impact on the fundamental semiconductor properties such as carrier effective masses.

Introduction

Nitride materials find diverse uses in industry and research. The nitrides of silicon and titanium are used extensively as wear-resistant coatings, and established semiconductor uses of nitrides include the group III nitrides,[1,2] used as light-emitting diodes (LEDs) and solar absorbers, and silicon nitride, which is used as an antireflective layer in silicon photovoltaics. Nitride materials with emerging or potential optoelectronic applications include tantalum nitride, which has been used as an absorber in water splitting,[3] copper nitride, which has been predicted to possess electronic tolerance to physical defects and thus be suitable for photovoltaics,[4] and solid solutions of the group IV spinels, which have been suggested as tunable band gap materials for LEDs.[5] Group IV nitrides commonly take the form IV_3N_4, and they display diverse properties including predictions of superhardness in carbon nitride,[6] industrially useful wear resistance in silicon nitride,[7] catalytic activity in germanium nitride,[8] and a band gap in the visible range in tin nitride.[5] Due to the visible band gap, combined with its composition of abundant elements, we were motivated to study Sn_3N_4 for solar energy conversion.

Tin nitride, Sn_3N_4, is known to be a metastable semiconducting material that assumes the spinel structure.[9] Limited literature data exists on the semiconducting properties of this material: It is n-type, with reported carrier densities of ~10^{20} cm^{-3} and mobilities of ~3 cm^2/Vs.[10] The optical absorption onset has been observed at 1.94 to 2.25 eV[11] (for material prepared by chemical vapor deposition) and 1.5 eV[10] (for material prepared by reactive sputtering). Several computational studies on tin nitride exist, reporting the electronic band gap at 1.5 eV by density functional theory (DFT),[5] 1.29 eV (by othogonalized linear combination of atomic orbitals within DFT),[12] and 1.15 eV (by local density approximation).[13] A non-crystalline phase of tin nitride has been reported by several groups[11,14,15] and may contain reduced forms of tin such as Sn(0) and Sn(II) compared to the ideal Sn(IV) material.[16] Tin nitride is not used industrially, but it has been suggested as a material for light-emitting diodes,[5] and exploitation of its metastable character has been demonstrated as means to produce small metallic Sn(0) features such as interconnects in microelectronics.[17] Researchers have investigated the photoelectrochemical activity of the amorphous phase, finding it could potentially serve as a photo-catalyst for water oxidation.[18] Another application that has been probed is lithium ion batteries, where the crystalline Sn_3N_4 decomposed and metallic Sn-Li alloys were found to be the electrochemically active phase.[19]

To address the challenges posed by this material's metastability and explore its semiconducting properties further, it would be interesting to develop new synthetic schemes that control the crystal phase, composition, and semiconducting properties generally. Tin nitride has been most frequently prepared by reactive sputtering of tin metal in a nitrogen-containing atmosphere.[10,15,17,20–23] Sn_3N_4 films can also be obtained by chemical vapor deposition (CVD) from halide[24] and organometallic[11] precursors. Bulk nanocrystalline synthesis can be accomplished by solid-state ion-exchange,[25] by thermal decomposition of a tin amide imide prepared in liquid ammonia,[26] and by wet-chemical methods from halide salts.[27] In contrast to these methods, ourselves and others have been pursuing high-throughput combinatorial synthesis and characterization,[28,29] a technique that becomes even more powerful when combined with computational studies and more detailed characterization of a smaller set of samples. Our current high-throughput methodology involves thin film synthesis with composition[30,31] or growth conditions[32,33] varied spatially across a substrate followed by spatially-resolved characterization. This produces a large amount of data that we subsequently process in custom software routines. Combinatorial experiments produce a range of properties and synthetic boundaries, and the computational data provides a reference for the expected materials properties in the ideal defect-free crystalline structure.

In this work, we combine a computational study of spinel (γ) Sn_3N_4 with experimental thin film synthesis covering a wide range of growth conditions, followed by solid-state and electrochemical characterization. These experiments yielded tin nitride with a slow optical absorption onset, and the valence band maximum was measured to be 5.9-6.0 eV below vacuum. According to the computational results, tin nitride has a direct band gap of 1.54 eV and the large dispersion of the conduction band leads to a small electron effective mass, but the high density of states (DOS) at the valence band maximum leads to a large hole effective mass. The results are placed in context by investigating computationally both chemical and structural trends, considering additionally the Ge and Si nitrides, Si_3N_4 and Ge_3N_4, and three different structures, i.e., the α, β, and γ (spinel) polymorphs. (Note that all three polymorphs of Si_3N_4 and Ge_3N_4, are known experimentally but only the γ phase is known for Sn_3N_4.)

Methods

Thin films of crystalline Sn_3N_4 were synthesized by radio-frequency (RF) reactive sputtering of metallic tin targets in a nitrogen and argon atmosphere. The glass, silicon, and fluorinated tin oxide coated glass substrates were placed at a 45° angle to the target producing a gradient in target-substrate distance. Nitrogen was provided through an RF atom source to increase its reactivity. The deposition geometry is shown in Figure 1a. The films were characterized by X-ray diffraction, optical spectroscopy, and four-point probe at spatially resolved points on the substrate corresponding to different growth conditions, and the resulting large amount of data was processed using custom-written a software package within Igor Pro. In order to obtain high activity of nitrogen[32] needed to keep tin in its fully-oxidized Sn(IV) state, the substrates were not actively heated. Additional details about our general approach can be found in our prior publications[32,34] and specific experimental details are included in the supplementary information.

We characterized a smaller set of samples by Rutherford backscattering (RBS) for elemental analysis, air photoemission spectroscopy (aPES) to determine valence band position, Kelvin probe to measure work function, and scanning electron microscopy (SEM) to determine film morphology. Hall effect and temperature-dependent conductivity measurements were used to determine electrical properties. Electrochemical methods were used to test the minority carrier diffusion length by generating electron-hole pairs with chopped AM 1.5 illumination on the front and back surfaces of the Sn_3N_4/fluorinated tin oxide (FTO)/glass devices. Devices were immersed in buffered solution with SO_3^{2-} as a sacrificial hole acceptor. Front- and back-illuminated photocurrents were then compared to estimate the diffusion length. Additional characterization details are available in the supplementary information.

Relaxed structures and total energies of all materials were obtained by Density Functional Theory (DFT) calculations[35] in the generalized gradient approximation, using a 28 atom cell for α structures and 14 atom cells for β, and γ structures. The formation enthalpies of the compounds were obtained using the Fitted Elemental Reference Energies (FERE).[36] The electronic structure and optical properties were obtained by DFT+GW.[37,38] The electron effective masses were obtained directly from the curvature of the conduction band. Due to the degeneracy and anisotropy of the valence band, we give the density of states (DOS) effective masses for the holes instead, using T = 1000 K for the DOS integration.[39,40] The absorption coefficient was calculated from the GW band-structure using the bootstrap kernel from Sharma *et al.*[41] to take

into account excitonic effects. The electron affinity and ionization potential were calculated by combining DFT+GW with DFT slab calculations[42] for a (110) surface orientation, which is one of the predominate natural growth faces for spinels,[43] averaging over two non-equivalent surface terminations.

Results:

It was found that target-substrate distance (d_{TS}) has a dramatic influence on the properties of tin nitride. Long-range order, as observed by XRD, increases as d_{TS} decreases. This result is shown in Figure 1b. RBS, wide-scan XRD and SEM were used to characterize the crystalline materials

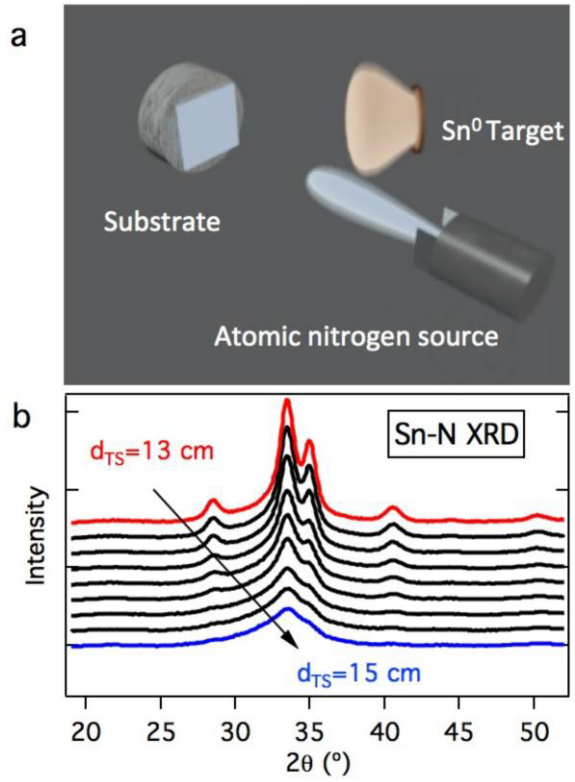

Fig. 3.1a: Schematic of combinatorial sputtering set-up. Fig. 3.1b: XRD patterns as a function of target-substrate distance.

further. Analysis of the RBS spectrum (See supplemental information Figure S1.) reveals an approximately stoichiometric sample with an Sn/N fraction of 0.78 ±0.03. A detectable but not quantifiable amount of oxygen was observed throughout the thickness of the film, and is likely responsible for the n-type conductivity observed through oxygen-on-nitrogen-site defects. Wider scan XRD and SEM are shown in Figure 2. The film adopted a strong but incomplete ⟨111⟩

crystallographic orientation compared to the calculated powder pattern. We note that the orientation observed in Fig. 2a is absent in Fig. 1b due to differences in data collection: our high-throughput XRD utilizes an area detector and integrates across φ and ω resulting in a more powder-like pattern and broader peaks. Grains were observed to be 50-100 nm in size by SEM, with some of the grains having pyramidal tops.

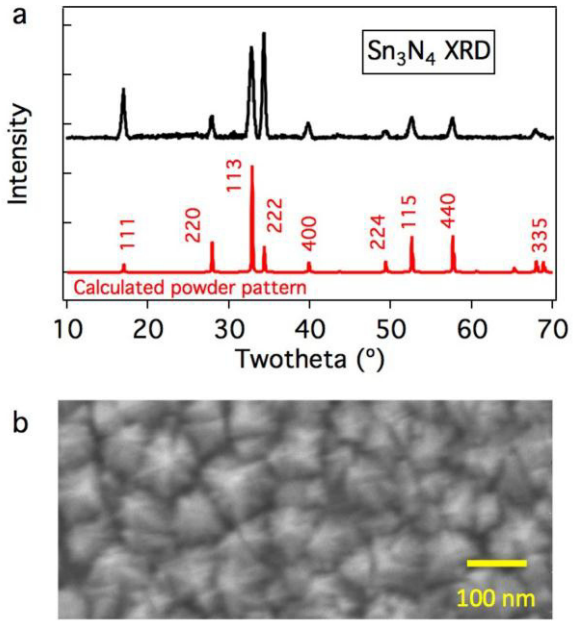

Fig. 3.2a: XRD of as-deposited film at d_{TS} = 13 cm with calculated powder pattern. Fig. 3.2b: SEM image of Sn_3N_4 film.

Optical spectroscopy placed the absorption onset (which we define as $\alpha > 5000$ cm^{-1}) at 1.6 eV, and temperature-dependent Hall measurements determined a carrier activation energy of 0.1-0.2 eV. The optical and Hall measurements are shown in Figure 3. The slope of the experimental optical absorption (Fig. 3a) is relatively slow for a direct gap semiconductor, reaching $6*10^4$ cm^{-1} at 2.6 eV, i.e., more than 1 eV above the calculated band gap. This slope is much slower compared to optoelectronic conversion materials such as CdTe, GaAs,[44] and $CuSbS_2$,[45] and leads to a yellow color in thinner films and a deep orange color for the thicker films (Fig. 3a inset). The calculated absorption spectrum follows the measured absorption coefficient closely, providing confidence that the predicted band gap of 1.54 eV is accurate. Films with low structural order (blue data in Fig. 1b and 3b) showed carrier concentrations as

high as 10^{20} cm^{-3} with mobilities of 0.4 cm^2/Vs. By reducing target-substrate distance and increasing crystallinity, we were able to reduce the carrier concentration to 10^{18} cm^{-3} and increase the mobility to 0.7-1.2 cm^2/Vs. This illustrates the importance of anion activity in the synthesis of metastable materials, as has been previously demonstrated for Cu_3N.[32] In the case of Cu_3N, increasing target-substrate distance led to lower chemical potentials of nitrogen and copper metal inclusions. Similar film reduction in tin nitride would lead to Sn(II) on Sn(IV) sites,

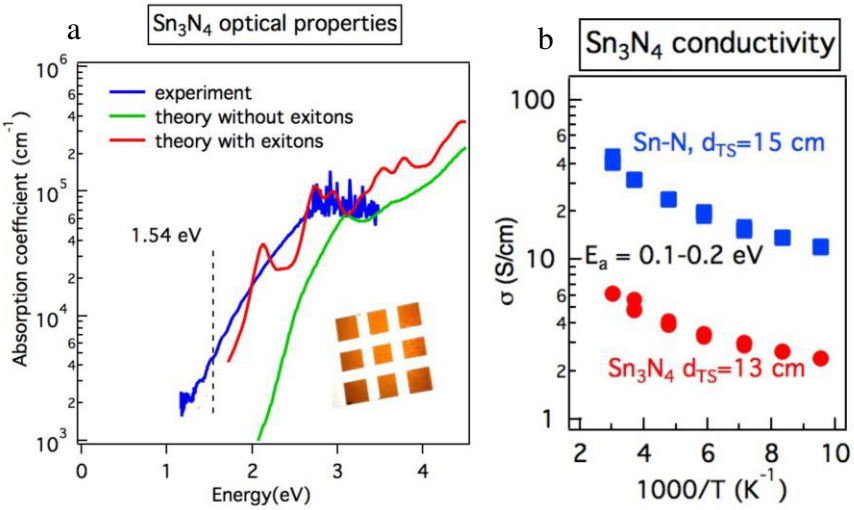

Fig. 3.3a: Optical properties of Sn_3N_4 films showing experimental (blue) and computational (red and green) data. Fig. 3.3a inset: photograph of the film with diffuse backlighting to show the deep orange color. Fig 3.3b: Temperature-dependent Hall measurements showing conductivity and carrier activation energies for amorphous (blue) and crystalline (red) material.

frustration of crystal growth, and high carrier concentration, consistent with our observations.

The work function of Sn_3N_4 was measured by kelvin probe as 4.7 eV and air photoemission determined the ionization potential of 5.9-6.0 eV. With appropriate references, both the ionization potential (IP) measurement and work function (WF) measurement determine energy levels with respect to vacuum, and allow us to estimate the position of the conduction band maximum, or electron affinity (EA) as:

$$EA = E_{vac} - E_{valence} + E_{gap} = IP + E_{gap} \qquad (1)$$

With E_{gap} approximated as the absorption onset of 1.6 eV and IP measured by air photoemission. Alternatively, the electron affinity can be calculated from the work function and carrier activation energy (E_a):

$$EA = E_{vac} - E_F + E_a \quad = WF + E_a \qquad (2)$$

Where E_F is the Fermi level measured as the work function by Kelvin probe. The IP and absorption measurements yield EA= 4.3 to 4.4 eV below vacuum from Eq. 1, whereas Kelvin probe data, Hall effect data, and Eq. 2 place the conduction band 4.5 to 4.6 eV below vacuum. This is good agreement from independent techniques and lends confidence to the measurements. The results are summarized in Table 1. The valence band position has good alignment for several photon-conversion applications such as photoelectrochemical water oxidation.

Table 1: Measured and calculated band positions of Sn_3N_4

Property	Experiment (air)	Theory (vacuum)
Band gap (eV)	--	1.54
IP (eV)	5.9-6.0	6.5
EA (eV)	4.3-4.6	5.0
WF (eV)	4.7	--

Given its valence band position, photoelectrochemical characterization was undertaken to evaluate the promise of Sn_3N_4 in the water oxidation half-reaction. A comparison of photocurrent generated from Sn_3N_4/FTO/glass devices immersed in an aqueous solution of sacrificial hole acceptor was used to elucidate the minority carrier diffusion length. As shown in Fig. 4, the quotient of back illumination/front illumination was plotted as a function of sample thickness to determine the minority carrier diffusion length. Back and front illumination produced roughly equal photocurrents in films with absorber layers up to 50 nm thick, and backside photocurrents decreased in thicker films, suggesting that many holes generated at the FTO/Sn_3N_4 interface were unable to migrate to Sn_3N_4/solution interface. Thus, in these devices, the minority carrier

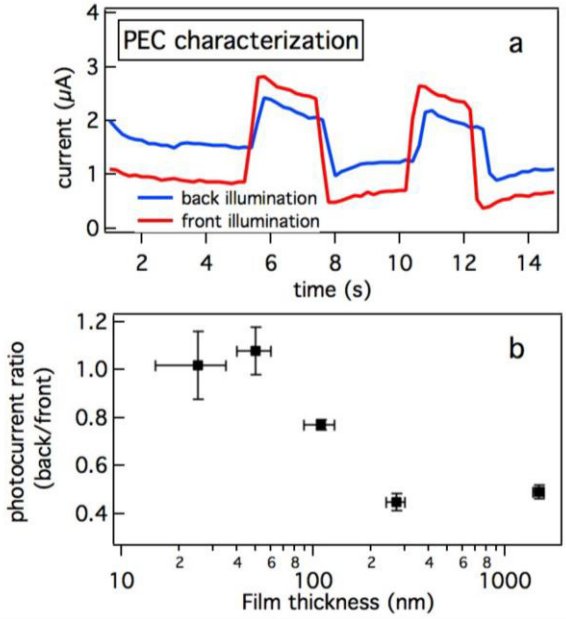

Fig. 3.4a: Photocurrent from a device of approximately 1 cm^2 area under chopped AM 1.5 illumination with sacrificial hole acceptor. Fig. 3.4b: Photocurrent ratio to determine minority carrier diffusion length.

diffusion length was between 50 and 100 nm.[46] Note that this is in the same order as the grains sizes. Thus, the material is probably limited by the small grain size, not fundamental transport properties. Due to the small photocurrent and small minority carrier diffusion length, the present Sn_3N_4 samples are not efficient for water splitting. A more detailed analysis of the charge generation, separation, and transport properties are required to understand the nature of the low photocurrents and small minority carrier diffusion length observed with sputter-deposited Sn_3N_4.

Though experimental results are always limited to the specific characteristics of the samples as synthesized, first-principles calculations allow us to understand the challenges and potential of a material in its defect-free form. The partial density of states of Sn_3N_4 calculated with DFT+GW is shown in Figure 5. The positions of the valence and conduction bands are aligned with respect to the vacuum level using the potential step calculated at a (110) surface.[42] For comparison, the experimental band positions (cf. Table 1) are also shown in Figure 5.

The high density of states due to N-*p* and Sn-*d* contributions in the vicinity of the valence band maximum results in a large calculated hole effective mass of $m_h^* = 12.9\ m_0$. Close to the conduction band minimum, the very small density of states originating from Sn-*s* and N-*s* contributions results in a small calculated electron effective mass of only $m_e^* = 0.18\ m_0$. The conduction band character is similar in related oxide materials, such as SnO_2 and ZnO, which are

well known for their excellent electron-transport properties in transparent conducting oxides.[47] Notably, the value of m_e* in Sn_3N_4 is still smaller than in SnO_2 and ZnO, for which we calculated m_e* = 0.24 and 0.27 m_0, respectively, for comparison.

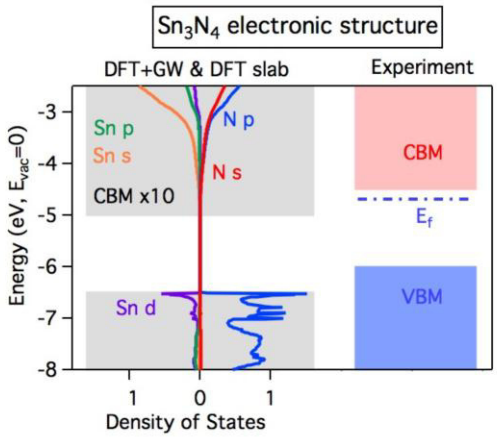

Fig. 3.5: Calculated electronic structure (left) and experimental band positions (right) of Sn_3N_4.

The calculated ionization potential is about 0.5 eV larger than that deduced from experimental data. However, the surface ionization potential is fairly sensitive to the detailed surface structure, and varies, e.g., with surface orientation,[48,49] or the presence of surface oxidation. In Ref (4), it was found for Cu_3N that a partially oxidized surface is particularly stable minimizing the surface energy. The relatively high energy of 136 meV/Å^2 calculated for the present (110) surface suggests that similar oxidation effects are likely to occur for Sn_3N_4, and should be considered in more detailed future studies of the Sn_3N_4 surface properties.

Considering the very small electron effect mass, the relatively low observed majority charge carrier mobility of ~1 cm^2/Vs is indicative of a very short time between scattering events, according to the equation:[50]

$$\mu_e = e\,\tau_e / m_e^* \qquad (3)$$

Where μ is mobility, m_e^* is the effective mass, e is the charge of the electron, and τ_e is the time between scattering events. τ_e decreases as defect concentration increases, with a material- and defect-specific functional relationship. In this case, τ_e = 0.1 fs. For comparison we note that fluorinated tin oxide (m_e^* = 0.24 m_0) has an ionized impurity density of >10^{20} cm^{-1} while maintaining an electron mobility of ~20 cm^2/Vs.[47] Thus, increasing the anion activity

successfully reduced the carriers in Sn_3N_4 but may not have reduced compensated defects (scattering centers which do not contribute carriers.) The small grains observed in SEM (Fig. 2) may also limit mobility through grain-boundary scattering.

Scattering of the minority carrier would occur by different mechanisms than the scattering of electrons, but the prediction of heavy holes and the observation of numerous defects and small grains should severely limit the minority carrier diffusion length, as observed here. The experimental results for crystalline Sn_3N_4 are summarized in Table 2.

Table 2: Compilation of experimental results for spinel Sn_3N_4.

Property	Value
Ionization potential	5.9-6.0 eV
Electron affinity	4.3-4.6 eV
Carrier activation energy	0.1-0.2 eV
Carrier concentration	10^{18} e^-/cm^3
Carrier mobility	0.7-1.2 cm^2/Vs
Optical onset ($\alpha > 5000$ cm^{-1})	1.6 eV

Discussion

To elucidate the origins of the high hole effective mass, we compared Sn_3N_4 to related materials. Another metastable nitride (Cu_3N) is compared to the thermodynamically stable GaN (which shares the anion with Sn_3N_4) and the stable SnO_2 (shared cation) in Table 3. Cu_3N, GaN, and SnO_2 are calculated by the same method used to obtain Sn_3N_4 values and compare favorably with literature values.[51,52] From the data in Table 3, it is clear that structure, and not only elements, plays a major role in determining the DOS at the band extrema and thus the carrier effective masses.

More insight into structure-composition-property relationships can be obtained by placing spinel Sn_3N_4 in the context of other IV_3N_4 materials. Silicon and germanium nitrides both form the spinel (γ) structure as one of their polymorphs,[53,54] thus allowing comparison between materials with different cations but the same structure. To compare the same elements

Table 3: Coordination environments and calculated carrier effective masses of Sn_3N_4 and related materials.

Compound	Cation site	Anion site	m_h^* (m_0)	m_e^* (m_0)
Sn_3N_4	Octahedral, tetrahedral	Tetrahedral	12.9	0.18
Cu_3N	Linear	Octahedral	2.3	0.73
GaN	Tetrahedral	Tetrahedral	1.7	0.21
SnO_2	Octahedral	Trigonal planar	1.2	0.24

in different structures, the α (hexagonal structure with tetrahedrally coordinated cations and trigonally coordinated anions) and β (trigonal structure with tetrahedrally coordinated cations and trigonally coordinated anions) polymorphs are calculated as well. These materials are known for Si and Ge, but have not been observed for Sn. The results are reported in Table 4, and the trends of the calculated hole masses are illustrated graphically in Figure 6. Relatively heavy hole masses ($m_h^* > 4\ m_0$) are observed in all of the γ structures, with increasing masses down the period (Si → Ge → Sn). The large hole masses result from a small dispersion of the valence band and similar VBM energies at different high-symmetry points in the Brillouin zone. The α and β forms of silicon, germanium, and tin nitride all show hole effective masses less than 4 m_e, without a clear periodic trend. On the other hand, the electron effective masses tend to decrease down the group in the periodic table, which follows the expectation from general trends in various semiconductor materials.[55]

Table 4: Calculated semiconductor properties for IV_3N_4 polymorphs. Values from DFT+GW and FERE.

Property	α	β	γ
Hole mass (m_0)			
Si_3N_4	2.47	1.47	4.11
Ge_3N_4	2.44	3.90	9.31
Sn_3N_4	2.55	3.46	12.9
Electron mass (m_0)			
Si_3N_4	1.00	0.76	0.52
Ge_3N_4	0.30	0.28	0.54

Sn_3N_4	0.19	0.17	0.18
Band gap (direct gap) (eV)			
Si_3N_4	6.77 (6.85)	6.46 (6.70)	5.09 (5.16)
Ge_3N_4	4.36 (4.41)	4.25 (d)	3.50 (3.52)
Sn_3N_4	1.53 (1.54)	1.34 (d)	1.54 (d)
Enthalpy of formation (eV/formula unit)			
Si_3N_4	-8.22	-8.22	-7.21
Ge_3N_4	-1.04	-1.02	-0.29
Sn_3N_4	2.31	2.31	1.56

The thermodynamic stability increases up the period with the α and β forms being very close in energy, which is consistent with the literature for Si_3N_4 and Ge_3N_4.[56] The α and β forms of Sn_3N_4

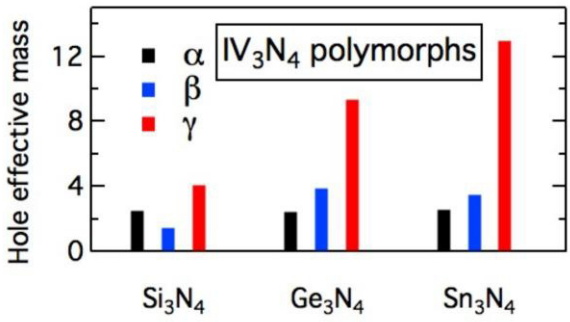

Fig. 3.6: Hole effective masses of group IV nitride polymorphs.

are significantly less stable than the γ structure, perhaps explaining why only the γ structure has been observed experimentally. The chemical trends of the band gaps follow that of other semiconductor systems, increasing up the period from a 1.34 eV direct gap in β-Sn_3N_4 to a 6.77 eV indirect gap in α-Si_3N_4. Structurally, the β structures have a slightly smaller gap than the α structures, and for Si_3N_4 and Ge_3N_4, the γ structures have a significantly reduced gap.

Overall, the results suggest that heavy holes in spinel Sn_3N_4 will make n-type minority-carrier devices challenging, and that any future application of Sn_3N_4 should look to take advantage of its low electron effective mass. Growing high-quality and large-grained Sn_3N_4 as a p-type material could accomplish this, with the very small electron effective mass facilitating large minority carrier diffusion lengths. Beyond binary Sn_3N_4, semiconducting properties could be customizable within IV_3N_4 alloy systems. For example it could be possible to stabilize the β phase of Sn_3N_4 by mixing in silicon, thereby reducing the hole effective masses and increasing

the band gap, and amorphous alloys may display smooth changes in properties as a function of composition. Such musings justify further computational and perhaps experimental exploration of this material system.

Conclusions

Sn_3N_4 and the IV_3N_4 polymorphs are an interesting and diverse set of compounds. The computational part of this works gives detailed band-structure and optical properties, and describes the chemical and structural trends in the IV_3N_4 family. Experimentally, for Sn_3N_4, we find that crystalline materials can be produced with small target-substrate distances. We determined a band gap of 1.54 eV, an ionization potential of 5.9-6.0 eV, and predict a large hole effective mass and a small electron effective mass. The carrier concentration was as low as 10^{18} cm^{-3} (n-type), with an electron mobility of ~1 cm^2/Vs and a minority carrier diffusion length of 50-100 nm. Sn_3N_4 would be an interesting p-type material, with the small electron effective mass leading to large minority carrier diffusion lengths. This works places spinel tin nitride in the context of the more-studied silicon and germanium nitrides, and the alloy systems between these materials may provide fruitful research by producing tunable properties.

References

(1) Strite, S.; Lin, M. E.; Morkoc, H. Progress and Prospects for GaN and the III-V Nitride Semiconductors. *Thin Solid Films* **1993**, *231*, 197–210.

(2) Akasaki, I. Nitride Semiconductors--Impact on the Future World. *J. Cryst. Growth* **2002**, *237-239*, 905–911.

(3) Ma, Y.; Oleynikov, P.; Li, Y.; Zhang, L.; Torres-pardo, A.; Gonza, J. M.; Terasaki, O.; Asahina, S.; Shima, M.; Cha, D.; *et al.* Cobalt Phosphate-Modified Barium-Doped Tantalum Nitride Nanorod Photoanode with 1.5% Solar Energy Conversion Efficiency. **2013**, 1–2.

(4) Zakutayev, A.; Caskey, C. M.; Fioretti, A. N.; Ginley, D. S.; Vidal, J.; Stevanović, V.; Tea, E.; Lany, S. Defect Tolerant Semiconductors for Solar Energy Conversion. *J. Phys. Chem. Lett.* **2014**, *In press*.

(5) Boyko, T. D.; Hunt, A.; Zerr, A.; Moewes, A. Electronic Structure of Spinel-Type Nitride Compounds Si3N4, Ge3N4, and Sn3N4 with Tunable Band Gaps: Application to Light Emitting Diodes. *Phys. Rev. Lett.* **2013**, *111*, 097402.

(6) Liu, A. Y.; Wentzcovitch, R. M. Stability of Carbon Nitride Solids. *Phys. Rev. B* **1994**, *50*, 10362–10365.

(7) Ceradyne's Ceralloy® Silicon Nitride http://www.ceradyne.com/uploads/Brochures/SiN_Brochure.pdf (accessed Jun 11, 2014).

(8) Sato, J.; Saito, N.; Yamada, Y.; Maeda, K.; Takata, T.; Kondo, J. N.; Hara, M.; Kobayashi, H.; Domen, K.; Inoue, Y. RuO 2 -Loaded B-Ge3N4 as a Non-Oxide Photocatalyst for Overall Water Splitting. *J. Am. Chem. Soc.* **2005**, *127*, 4150–4151.

(9) Scotti, N.; Kockelmann, W.; Senker, J. Sn3N4, Ein Zinn (IV)-Nitrid - Synthese Und Erste Strukturbestimmung Einer Bina È Ren Zinn-Stickstoff-Verbindung. *Z. Anorg. Allg. Chem.* **1999**, *625*, 1435–1439.

(10) Inoue, Y.; Nomiya, M.; Takai, O.; Processing, M. Physical Properties of Reactive Sputtered Tin- Nitride Thin Films. *Vacuum* **1998**, *51*, 673–676.

(11) Gordon, R. G.; Hoffman, D. M.; Riaz, U. Low-Temperature Atmospheric Pressure Chemical Vapor Deposition of Polycrystalline Tin Nitride Thin Films. *Chem. Mater.* **1992**, *4*, 68–71.

(12) Ching, W. Y.; Mo, S.-D. Prediction of Spinel Structure and Properties of Single and Double Nitrides. *Phys. Rev. B* **2001**, *63*, 064102.

(13) Huang, M.; Feng, Y. P. Theoretical Prediction of the Structure and Properties of Sn3N4. *J. Appl. Phys.* **2004**, *96*, 4015–4017.

(14) Maruyama, T.; Morishita, T. Copper Nitride Thin Films Prepared by Radiofrequency Reactive Sputtering. *J. Appled Phys.* **1995**, *78*, 1–5.

(15) Kamei, R.; Migita, T.; Tanaka, T.; Kawabata, K. Effect of D.c. Bias on the Deposition Rate Using R.f. - D.c. Coupled Magnetron Sputtering for SnNx Thin Films. *Vacuum* **2000**, *59*, 764–770.

(16) Lützenkirchen-Hecht, D.; Frahm, R. Structure of Reactively Sputter Deposited Tin-Nitride Thin Films: A Combined X-Ray Photoelectron Spectroscopy, in Situ X-Ray Reflectivity and X-Ray Absorption Spectroscopy Study. *Thin Solid Films* **2005**, *493*, 67–76.

(17) Maruyama, T.; Morishita, T. Copper Nitride and Tin Nitride Thin Films for Write-Once Optical Recording Media. *Appl. Phys.* **1996**, *69*, 890–891.

(18) Lindgren, T.; Larsson, M.; Lindquist, S.-E. Photoelectrochemical Characterisation of Indium Nitride and Tin Nitride in Aqueous Solution. *Sol. Energy Mater. Sol. Cells* **2002**, *73*, 377–389.

(19) Park, K. S.; Park, Y. J.; Kim, M. K.; Son, J. T.; Kim, H. G.; Kim, S. J. Characteristics of Tin Nitride Thin-Film Negative Electrode for Thin-Film Microbattery. *J. Power Sources* **2001**, *103*, 67–71.

(20) Maruyama, T.; Morishita, T. Tin Nitride Thin Films Prepared by Radio-Frequency Reactive Sputtering. *J. Appl. Phys.* **1995**, *77*, 6641–6645.

(21) Lima, R. S.; Dionisio, P. H.; Schreiner, W. H. Magnetron Sputtered Tin Nitride. *Solid State Commun.* **1991**, *79*, 395–398.

(22) Lima, R. S.; Dionisio, P. H.; Moro, J. T.; Schreiner, W. H. Thermal Evolution of Tin Nitride Obtained By Reactive Sputtering. *Hyperfine Interact.* **1994**, *83*, 315–319.

(23) Maya, L. Deposition of Crystalline Binary Nitride Films of Tin, Copper, and Nickel by Reactive Sputtering. *J. Vac. Sci. Technol. A* **1993**, *11*, 604–608.

(24) Takahashi, N.; Terada, K.; Nakamura, N. Growth of Tin Nitride Thin Films by Atmospheric Pressure Chemical Vapor Deposition Using a Halide Source. *J. Mater. Sci. Lett.* **2001**, *20*, 227–228.

(25) Shemkunas, M. P.; Wolf, G. H.; Leinenweber, K.; Petuskey, W. T. Rapid Synthesis of Crystalline Spinel Tin Nitride by a Solid-State Metathesis Reaction. *J. Am. Ceram. Soc.* **2002**, *85*, 101–104.

(26) Maya, L. Preparation of Tin Nitride via an Amide Imide Intermediate. *Inorg. Chem.* **1992**, *31*, 1958–1960.

(27) Lützenkirchen-hecht, D.; Scotti, N.; Chemie, F.; Dortmund, U. XAFS Investigations of Tin Nitrides. *J. Synchrotron Radiat.* **2001**, *8*, 698–700.

(28) Koinuma, H.; Takeuchi, I. Combinatorial Solid-State Chemistry of Inorganic Materials. *Nat. Mater.* **2004**, *3*, 429–438.

(29) Takeuchi, I.; van Dover, R. B.; Koinuma, H. C Ombinatorial Synthesis and Evaluation of Functional Inorganic Materials Using Thin-Film Techniques. *MRS Bull.* **2002**, 301–308.

(30) Zakutayev, A.; Zhang, X.; Nagaraja, A.; Yu, L.; Lany, S.; Mason, T. O.; Ginley, D. S.; Zunger, A. Theoretical Prediction and Experimental Realization of New Stable Inorganic Materials Using the Inverse Design Approach. *J. Am. Chem. Soc.* **2013**, *135*, 10048–10054.

(31) Zakutayev, A.; Paudel, T. R.; Ndione, P. F.; Perkins, J. D.; Lany, S.; Zunger, A.; Ginley, D. S. Cation off-Stoichiometry Leads to High P-Type Conductivity and Enhanced Transparency in Co2ZnO4 and Co2NiO4 Thin Films. *Phys. Rev. B* **2012**, *85*, 085204.

(32) Caskey, C. M.; Richards, R. M.; Ginley, D. S.; Zakutayev, A. Thin Film Synthesis and Properties of Copper Nitride, a Metastable Semiconductor. *Mater. Horizons* **2014**.

(33) Subramaniyan, A.; Perkins, J. D.; O'Hayre, R. P.; Lany, S.; Stevanovic, V.; Ginley, D. S.; Zakutayev, A. Non-Equilibrium Deposition of Phase Pure Cu2O Thin Films at Reduced Growth Temperature. *APL Mater.* **2014**, *2*, 022105.

(34) Perkins, J.; Paudel, T.; Zakutayev, a.; Ndione, P.; Parilla, P.; Young, D.; Lany, S.; Ginley, D.; Zunger, a.; Perry, N.; *et al.* Inverse Design Approach to Hole Doping in Ternary Oxides: Enhancing P-Type Conductivity in Cobalt Oxide Spinels. *Phys. Rev. B* **2011**, *84*, 1–8.

(35) Kresse, G.; Joubert, D. From Ultrasoft Pseudopotentials to the Projector Augmented-Wave Method. *Phys. Rev. B* **1999**, *59*, 1758–1774.

(36) Stevanović, V.; Lany, S.; Zhang, X.; Zunger, A. Correcting Density Functional Theory for Accurate Predictions of Compound Enthalpies of Formation: Fitted Elemental-Phase Reference Energies. *Phys. Rev. B* **2012**, *85*, 115104.

(37) Hedin, L. New Method for Calculating the One-Particle Green's Function with Application to the Electron-Gas Problem. *Phys. Rev.* **1965**, *139*, 796–822.

(38) Shishkin, M.; Kresse, G. Implementation and Performance of the Frequency-Dependent GW Method Withen the PAW Framework. *Phys. Rev. B* **2006**, *74*, 1–13.

(39) Ottaviani, G.; Reggiani, L.; Canali, C.; Nava, F.; Alberigi-Quaranta, A. Hole Drift Velocity in Silicon. *Phys. Rev. B* **1975**, *12*, 3318–3328.

(40) Trimarchi, G.; Peng, H.; Im, J.; Freeman, A. J.; Zunger, A. Using Design Principles to Systematically Plan the Synthesis of Hole-Conducting Transparent Oxides : Cu3VO 4 and Ag3VO4 as a Case Study. *Phys. Rev. B* **2011**, *84*, 1–14.

(41) Sharma, S.; Dewhurst, J. K.; Sanna, A.; Gross, E. K. U. Bootstrap Approximation for the Exchange-Correlation Kernel of Time-Dependent Density-Functional Theory. *Phys* **2011**, *186401*, 1–5.

(42) Stevanović, V.; Lany, S.; Ginley, D. S.; Tumas, W.; Zunger, A. Assessing Capability of Semiconductors to Split Water Using Ionization Potentials and Electron Affinities Only. *Phys. Chem. Chem. Phys.* **2014**, *16*, 3706–3714.

(43) Henrich, V. E.; Cox, P. *The Surface Science of Metal Oxides*; Cambridge University Press: Cambridge, 1994.

(44) Bube, R. H. *Photovoltaic Materials*; Newman, R. C., Ed.; Imperial College Press, 1998.

(45) Welch, A. A.; Zawadzki, P. P.; Lany, S.; Wolden, C. A.; Zakutayev, A. Self-Regulated Growth and Tunable Properties of CuSbS2 Solar Absorbers. *Submitted*.

(46) Seabold, J. A.; Zhu, K.; Neale, N. R. Efficient Solar Photoelectrolysis by Nanoporous Mo:BiVO4 through Controlled Electron Transport. *Phys. Chem. Chem. Phys.* **2014**, *16*, 1121–1131.

(47) Fortunato, E.; Ginley, D.; Hosono, H.; Paine, D. C. Transparent Conducting Oxides for Photovoltaics. *MRS Bull.* **2007**, *32*.

(48) Stevanović, V.; Hartman, K.; Jaramillo, R.; Ramanathan, S.; Buonassisi, T.; Graf, P. Variations of Ionization Potential and Electron Affinity as a Function of Surface Orientation: The Case of Orthorhombic SnS. *Appl. Phys. Lett.* **2014**, *104*, 211603.

(49) Bayer, T. J. M.; Br, J.; Albe, K.; Klein, A. Orientation Dependent Ionization Potential of In 2 O 3 : A Natural Source for Inhomogeneous Barrier Formation at. *J. Phys. Condens. Matter* **2011**, *23*, 1–8.

(50) Kittel, C. *Introduction to Solid State Physics*; Johnson, S., Ed.; Eighth Edi.; John Wiley & Sons, 2005.

(51) Dreyer, C. E.; Janotti, a.; Van de Walle, C. G. Effects of Strain on the Electron Effective Mass in GaN and AlN. *Appl. Phys. Lett.* **2013**, *102*, 142105.

(52) Button, K. J.; Fonstad, C. G.; Dreybrodt, W. Determination of the Electron Masses in Stannic Oxide by Submillimeter Cyclotron Resonance. *Phys. Rev. B* **1971**, *4*, 4539–4542.

(53) Zerr, A.; Miehe, G.; Serghiou, G.; Schwarz, M.; Kroke, E.; Riedel, R.; Fueß, H.; Kroll, P.; Boehler, R. Synthesis of Cubic Silicon Nitride. *Nature* **1999**, *400*, 340–342.

(54) Soignard, E.; Mcmillan, P. F. Raman Spectroscopy of Γ -Si 3 N 4 and Γ -Ge 3 N 4 Nitride Spinel Phases Formed at High Pressure and High Temperature : Evidence for Defect Formation in Nitride Spinels. *Chem. Mater.* **2004**, *16*, 3533–3542.

(55) Yu, P.; Cardona, M. *Fundamentals of Semiconductors*; 4th ed.; Springer-Verlag: Heidelberg, 1996.

(56) Wnag, H.; Chen, Y.; Kaneta, Y.; Iwata, S. First-Principles Investigation of the Structural , Electronic and Optical Properties of Olivine-Si3N4 and Olivine-Ge3N4. *J. Phys. Condens. Matter* **2006**, *18*, 10663–10676.

CHAPTER 4 OBSERVATION OF NEW CRYSTALLINE MATERIAL IN THE TIN NITRIDE SYSTEM

Christopher M. Caskey,[1,2] Chilan Ngo,[3] Xuiwen Zhang,[4] David S. Ginley,[1] John D. Perkins,[1] Stephan Lany,[1] Ryan M. Richards,[1,2] Andriy Zakutayev[1]

1) National Renewable Energy Laboratory
2) Department of Chemistry and Geochemistry, Colorado School of Mines
3) Department of Materials Science and Engineering, University of California Los Angeles
4) University of Colorado Boulder

This manuscript will be submitted to a peer-reviewed journal for publication. The first author was responsible for thin-film synthesis, a plurality of the measurements, and manuscript preparation.

Abstract

Materials discovery is central to the fields of chemistry and materials science, and centuries of work have left few binary compounds undiscovered. We report the first binary crystalline nitride containing Sn(II), a semiconductor having composition near SnN. Calculated low energy structures obtained by the structure prototype method indicate that a likely space group for this material is *P n m a* #62, though atomic position refinement was not possible. The material has a band gap between 1.5 and 2 eV, and n-type conductivity arising from 10^{20} carriers/cm^3 with mobility of 2 cm^2/Vs. A lower-defect version of this material would merit studies for optoelectronic energy conversion applications such as light emitting diodes, tandem photovoltaics, and photoelectrochemical water splitting.

Introduction

Discovery and cataloging of the unknown is central to all the physical sciences. Just as the cartographers, explorers and seamen of the last millennium searched for new lands and new navigable routes,[1] biology continues to push to new depths[2,3] and heights[4] find new creatures,[5] astronomers look for new planets,[6] telescope arrays listen for unknown intelligence,[7] chemists seek new reactions,[8–10] and the multi-decade, multi-billion euro search for the Higgs boson[11] proved Earnest Rutherford partially correct: even physics is stamp collecting.[12] Discovery of new condensed phases is an equally strong thrust in materials science,[13] with hundreds of new compounds being added to crystallographic databases annually.[14] The majority of these compounds are chemically complex ternary[15] and quaternary compounds or elemental and binary

phases obtained at high pressure.[16] Simple but unreported combinations and stoichiometries of elements exist, but discovery of new crystalline materials at mild synthesis conditions is rare. Even more unusual is for these discoveries to be made of abundant, common elements.

Tin compounds have useful and diverse properties: SnO_2 is used on huge commercial scales as the transparent conductor fluorinated tin oxide (FTO) and is also used as electrode materials for lithium ion batteries.[17] Tin sulfide (SnS) has been used as an absorber material in thin-film photovoltaics,[18] and SnF_2 is used extensively dentistry[19] and periodontry[20] to control hypersensitivity and gingivitis. The diversity of properties within this materials system is partially enabled by tin's ability to adopt both 2+ and 4+ oxidation states. Pure Sn(IV), pure Sn(II), and mixed Sn(IV)/Sn(II) compounds exist for the fluoride, oxide, and sulfide, while pure Sn(IV) and pure Sn(II) phases are documented for the phosphide.[21] Tin nitride, however, has only been observed as a Sn_3N_4, a Sn(IV) spinel,[22] and a related slightly reduced amorphous material.[23] Binary crystalline nitrides containing Sn(II) are unknown until now.

We report the discovery of a new phase of tin nitride with measured stoichiometry slightly tin rich of 1:1 ($SnN_{1-\delta}$) made by reactive sputtering. This new material is crystalline with cubic symmetry, and is a degenerate n-type semiconductor with optical absorption onset near 1.9 eV and carrier concentrations near 10^{20} cm^{-1}. The Earth abundance, ease of synthesis, and semiconducting properties make this material interesting not only from a fundamental science standpoint but also for potential practical applications.

Methods

Thin films of tin nitrides were grown on glass, silicon, and steel substrates by high-throughput combinatorial reactive sputtering of metallic tin targets in a nitrogen and argon atmosphere. Temperature and target-substrate distance (d_{TS}) were modulated as orthogonal variables such that each position on the sample experienced different growth conditions. Previous work on temperature gradient[24] and target-substrate distance gradient[25] films indicates that control of the cation oxidation state can be obtained by modulating these variables.

Films were characterized by X-ray diffraction (XRD), ultraviolet-visible spectroscopy (UV-Vis), scanning electron microscopy (SEM) transmission electron microscopy (TEM), and selected-area electron diffraction (SAED). Density-functional theory (DFT) structure prototype calculations were used to identify candidate structures.

Results and Discussion

Modulation of the anion chemical potential by changing target-substrate distance and substrate temperature had a dramatic affect on the resulting film. At the highest chemical potentials of nitrogen (low T_S and low d_{TS}), spinel Sn_3N_4 was formed. By increasing d_{TS}, the film became amorphous and presumably nitrogen poor. By increasing T_S to 450°C, crystalline tin metal (β-polytype) was formed alongside Sn_3N_4 spinel. Between these extremes exists a wide range of synthesis conditions where the new $SnN_{1-\delta}$ is observed. The thin film growth map is shown in Figure 1 alongside representative XRD patterns. In general, low target-substrate distances produced more highly crystalline material compared to long target-substrate distances, which

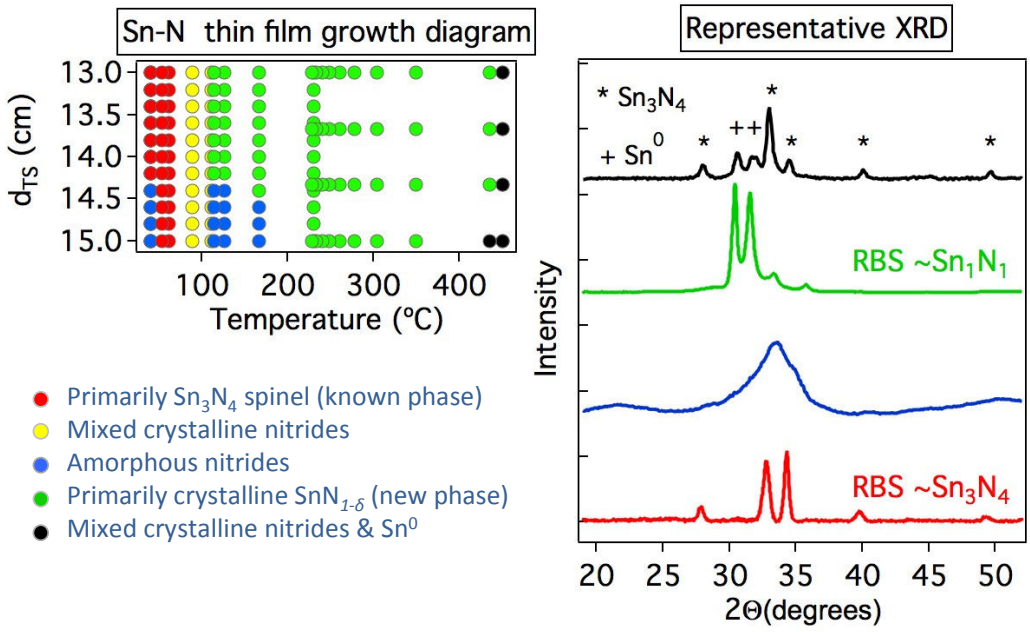

Fig. 4.1 left: Thin film growth diagram and (right) representative XRD for materials in the tin-nitrogen system.

produced more amorphous material. We note that the assigned growth map indicates the *primary* phase observed, and small amounts of neighboring phases can be found in the in the phase boundary regions. The highest-quality $SnN_{1-\delta}$ was produced near 350°C at small target substrate distances, and all additional characterization was performed on material grown at these conditions.

The stoichiometry of this new material was measured by Rutherford backscattering to be between SnN and Sn_9N_8. Differences between individual samples and instrumental uncertainty contributed to this range. No correlation between measured stoichiometries and variations in XRD patterns was observed. RBS spectra are shown in the supplementary information Figure S1.

Additional characterization of $SnN_{1-\delta}$ is shown in Figure 2. The X-ray diffraction peaks are primarily located in a few clusters, and peaks are somewhat broad indicating small grains, strained crystals, or both. Raman spectroscopy revealed several sharp resonances indicating high short-range order. The values of the Raman shifts are shown in Table 1. We note that these values are distinct from Raman shifts observed for Sn_3N_4,[26] confirming the novelty of this material. A table of XRD peak positions and corresponding inter-planar spacing is provided in Supplemental Information Table S1.

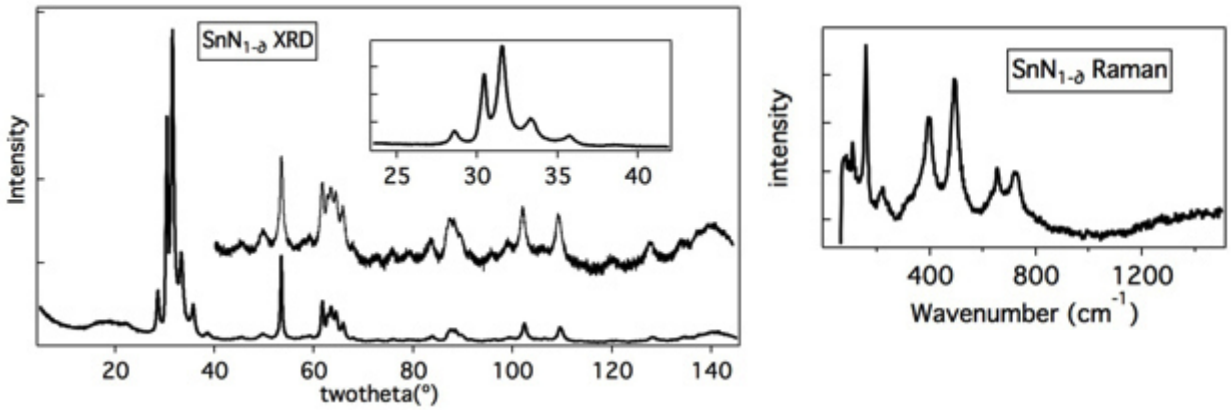

Fig. 4.2 left: XRD patterns of $SnN_{1-\delta}$ powders (Cu Kα radiation.) Bottom: wide scan with linear intensity axis. Middle: portion of the same pattern with log-scale intensity axis to show minor peaks. Inset: Expansion of cluster of peaks from 25 to 40°. Fig. 2 right: Raman spectrum of $SnN_{1-\delta}$ film.

Table 1: Raman shifts

Wavenumber (cm^{-1})	Intensity	Comment
108.0	Weak	Very sharp
156.6	Strong	Very sharp
222.2	Weak	Broad
293.2	Strong	Broad
490.4	Strong	Broad
652.2	Weak	Sharp
721.1	Weak	Broad

Electron microscopy was used to characterize films further. Clusters of grains are observed in Scanning electron microscopy (SEM). The clusters are 500-1000 nm long and composed of

grains of 100 nm or less. The size of the clusters increased with increasing film thickness, suggesting evolutionary growth of some columns over others. The SEM is shown in Figure 3. Transmission electron microcopy of samples viewed in cross-section after focused-ion beam lift

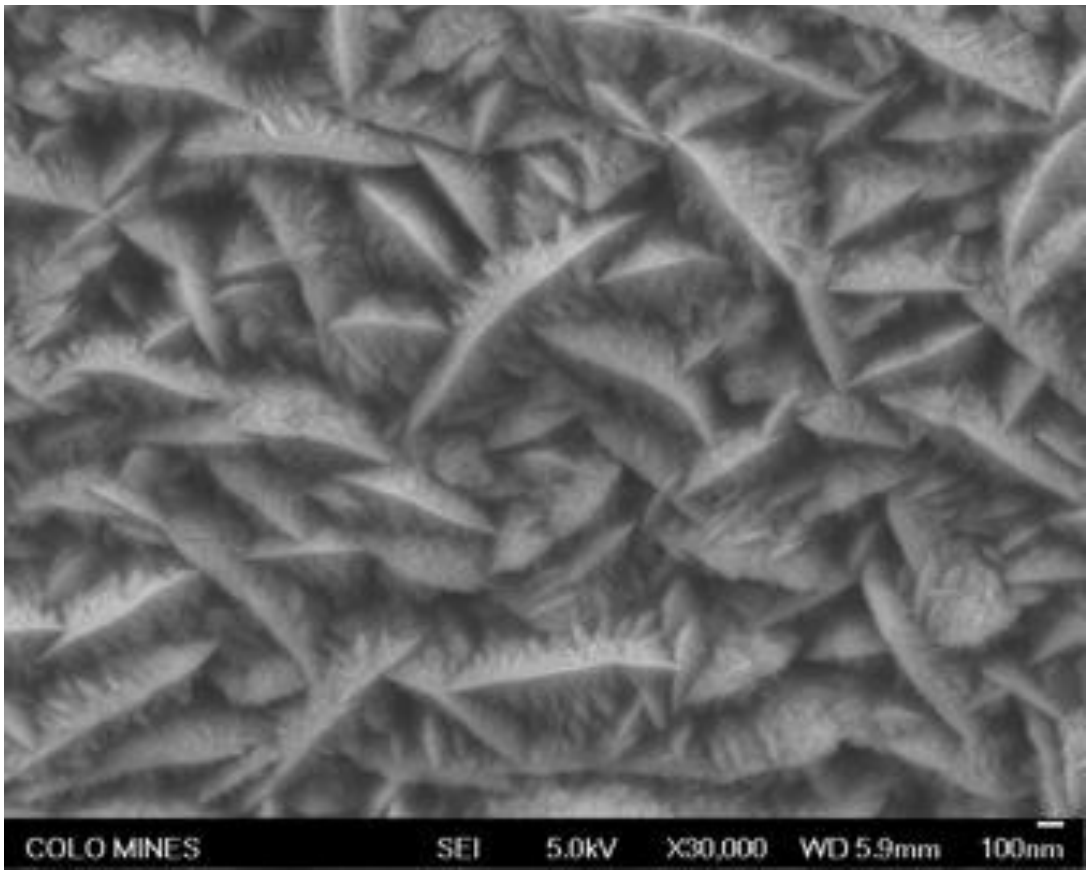

Fig. 4.3: SEM image of $SnN_{1-\delta}$ film grown on steel.

out columnar and dendritic superstructures assembled of small grains. This is shown in Figure 4. Some of these superstructures overgrew others, leading to the morphology observed by SEM (Figure 3). Low contrast material between the superstructures contained amorphous and crystalline phases visible by high-resolution TEM (HRTEM), (Figure 5) and variations in the quantity and composition of this amorphous material could be responsible for the variations in the bulk composition measured by RBS. The variation in composition at the microstructure level is unknown, because the nitrogen signal was out of range of our energy-dispersive X-ray spectroscopy instrument. Selected-area electron diffraction (SAED) measurements on the film

showed inner-planar spacings consistent with XRD spacings. The SEAD image is shown in Figure 6 and the spacings are shown in the Supplementary information Table S2.

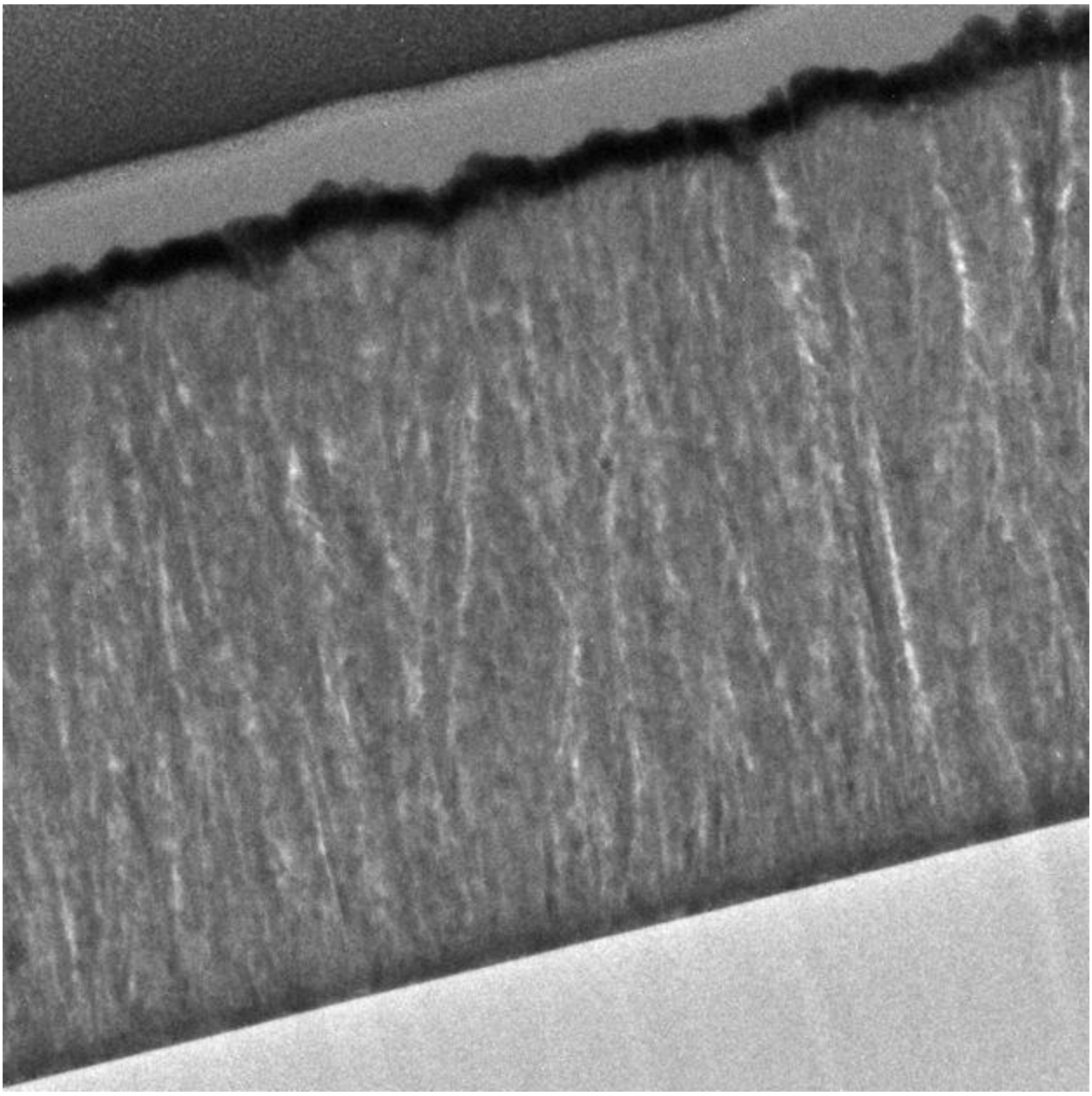

Fig. 4.4: TEM image of $SnN_{1-\delta}$ film in cross section prepared by focused ion beam method. The image is 1650 nm by 1650 nm.

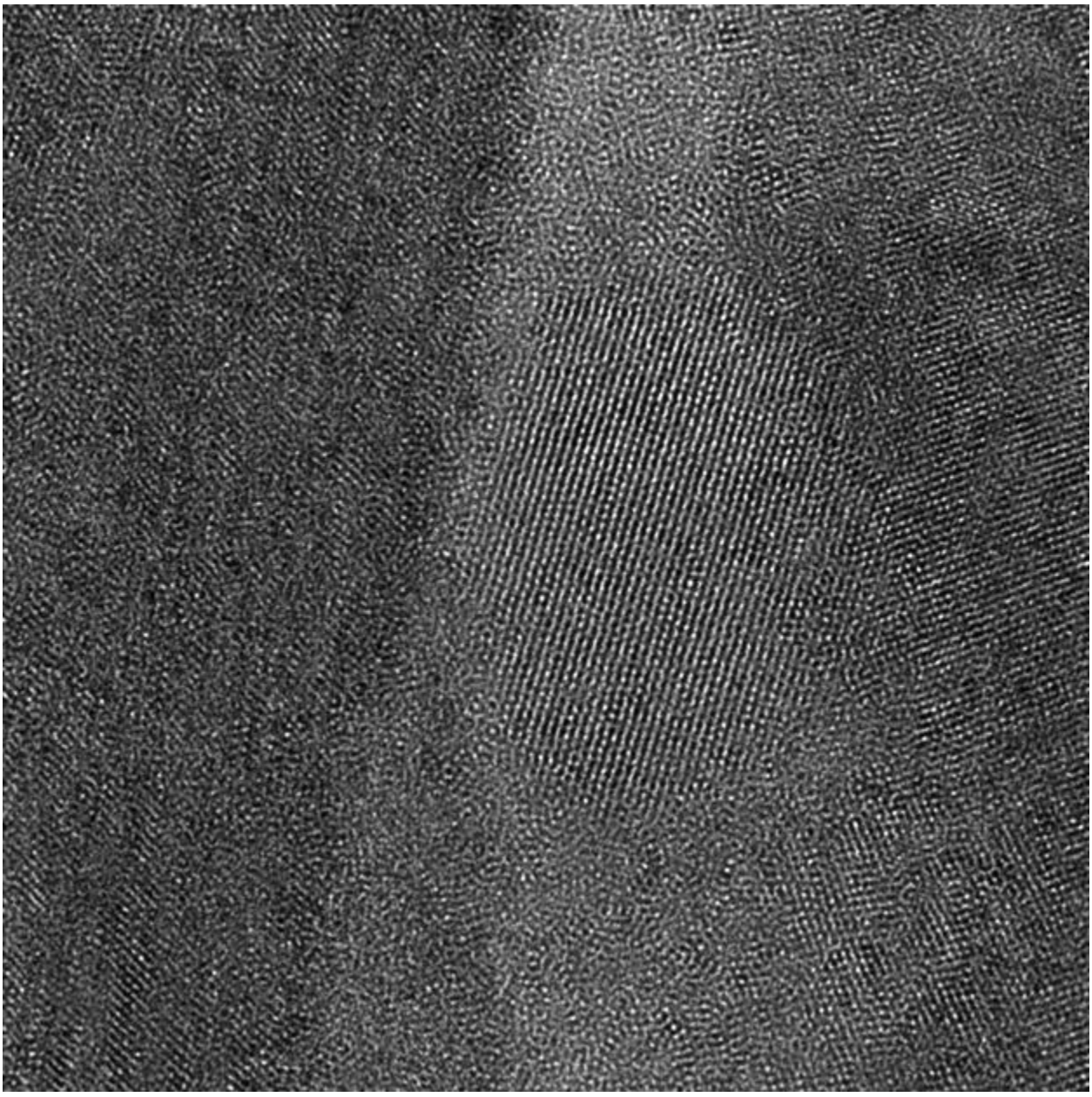

Fig. 4.5: HRTEM image of $SnN_{1-\delta}$ film in cross section prepared by focused ion beam method. The image is 35.83 nm by 35.83 nm.

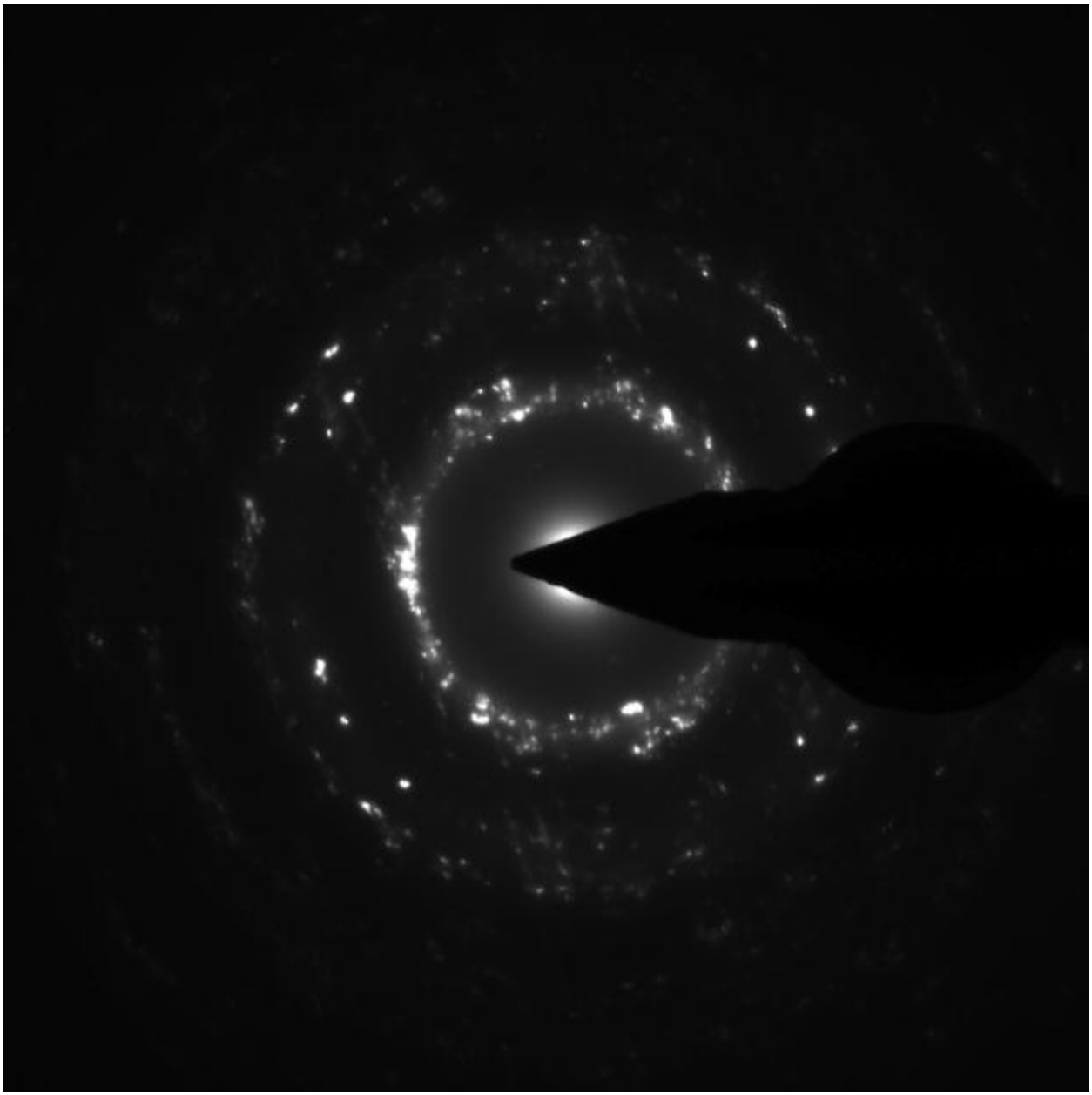

Fig. 4.6: SAED pattern of $SnN_{1-\delta}$ film.

$SnN_{1-\delta}$ has an absorption onset with a modest increase in absorption between 1 and 4 eV. The steepest point is near 1.95 eV, and the minimum is near 1 eV. In the infrared, we observed increased absorption resulting from free carrier plasmon resonance. The plasma frequency could not be reliably calculated because the low-energy maximum absorption is near the limit of our detector (grey box in Figure 7.) The presence of free carriers is also observed in temperature-dependent Hall measurements, where decreasing the temperature has almost no effect on the conductivity. Room temperature Hall effect measurements showed an n-type carrier concentration of $3*10^{20}$ cm^{-3} and a mobility of 2 cm^2/Vs. All of these observations are consistent with a degenerate n-type semiconductor.

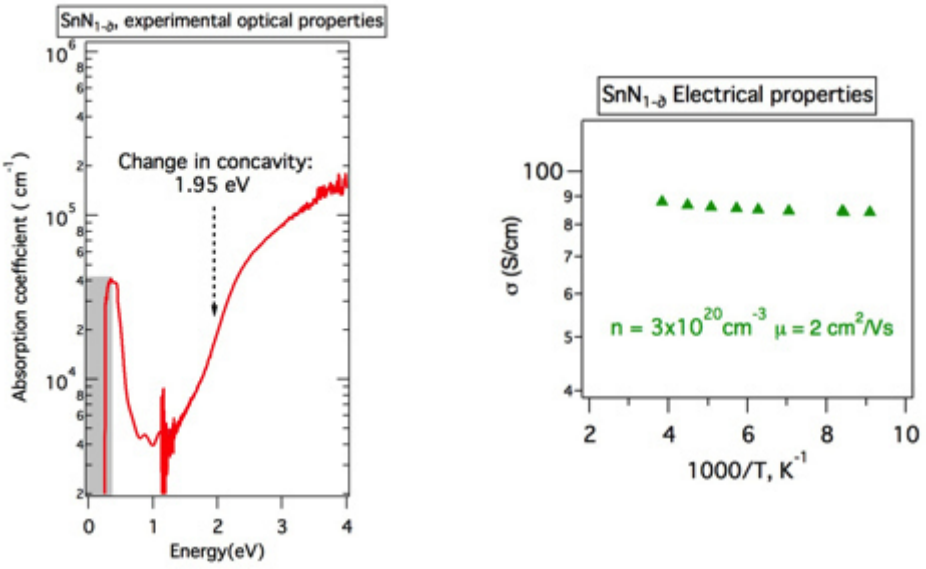

Fig. 4.7 left: Experimental optical properties. Fig. 7 right: Temperature dependent conductivity Text: room-temperature carrier concentration and mobility

Multiple undiscovered phases are possible in the tin-nitrogen system. Sn_3N_2 would be the pure tin (II) nitride, while Sn_9N_8 would be 2/3 tin (II) and 1/3 tin (IV). SnN is 1:1 Sn(II):Sn(IV), and other stoichiometries are possible. Confronted as we are with a large number of unassigned XRD peaks, it is prudent to assess whether all the reflections belong to one unknown material or multiple phases. Strategy 1 is to modulate growth conditions, thusly favoring one phase over another, and to verify by X-ray diffraction which reflections were increasing or decreasing. This is an attractive strategy because our combinatorial set-up allows rapid screening of different

growth conditions, as demonstrated in Figure 1a. Strategy 2 relies on the assumption that different materials will have different kinetic stabilities and thus different decomposition temperatures. Both strategies were employed. The results for Strategy 1 are shown in Supplemental Information Figure S2, and indicate that the majority of the variation in XRD patterns arising from changing growth conditions could be attributed to changes in the crystallographic orientation of the film. Strategy 2 possessed more utility. Assuming different materials have different kinetic stability, we performed a *high-throughput anneal* in which a homogenous sample was subjected to a temperature gradient in inert atmosphere. The affect of the anneal and phase evolution were observed by XRD, and are shown in Figure 8. The sample underwent an abrupt decomposition near 450°C. The decomposition products were tin metal and Sn_3N_4. All of the $SnN_{1-\delta}$ peaks disappeared very abruptly and in the same small temperature window. This result strongly infers that $SnN_{1-\delta}$ is a single phase. However, we note that the large number of diffraction spots in the SAED is unusual for a single-phase material, and two phasesw

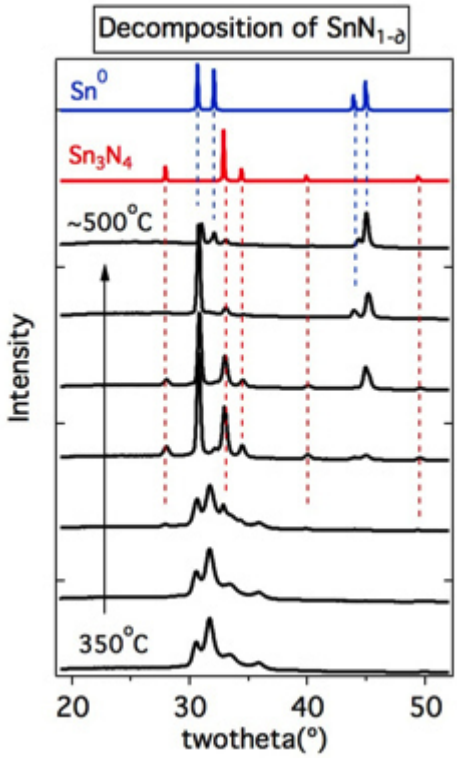

Fig. 4.8: high-throughput anneal of thin-film $SnN_{1-\delta}$ sample.

with similar kinetic stability may be present. Furthermore, we note that not all of the nitrogen escapes as N_2 during the initial decomposition, and that stepwise transformation into Sn_3N_4 is

seen in at least some of the material. This suggests that Sn_3N_4 is more thermodynamically stable than $SnN_{1-\delta}$.

First-principles calculations were undertaken to identify candidate structures for SnN. Two separate routes were attempted. The first approach is called Global Space Group Optimization, or GSGO.[27] In GSGO, the constituent atoms are placed randomly in a unit cell and allowed to move to a local or global energy minimum. Low energy forms are mixed, and the process repeated. This process is iterated many times to produce possible structures. In all cases, GSGO obtained the global energy minimum, which is phase-separated tin metal and nitrogen gas. We note that this is actually a correct result form theory: GSGO found the most stable structure, whilst the structure we are seeking is metastable. The second approach involves using structure prototypes.[28,29] In the structure prototypes approach, SnN is assumed to take the form ABX_2 where A=Sn, B=Sn, and X=N. Distinct Sn sites are assumed because the Sn(II) and Sn(IV) likely occupy different sites and because the large number of observed diffraction peaks indicates a low symmetry and makes an AX-type structure (which are typically high symmetry) unlikely. About 40 known ABX_2-type compounds are available as structure prototypes. Computationally, tin and nitrogen atoms are placed into the structure prototypes, and the atoms are allowed to relax to a local or global energy minimum. Of these 40, four structures had distinctly lower energies. Information on these structures is shown in Table 3. Of these four structures, the lowest energy structure contained nitrogen-nitrogen bonds, which are unlikely in our synthesis method and somewhat indicative of phase-separation. Two of the other structures showed promise. The XRD patterns of all four low energy structures were simulated using CrystalDiffract software, and one particular structure Pnma $CuBiS_2$-type was the best fit.

Table 3: Candidate structures for SnN obtained from DFT energy minimization of structure prototypes.

Structure prototype	Space group	ΔH_f (eV/formula unit)	Comments	XRD simulation
$CeNiC_2$	Amm2 #38	+0.41	Contains N-N bonds	Not promising
$CuBiS_2$	Pnma #62	+0.52	2 N sites, 2 Sn sites	Promising
Na_2AuSb	Cmcm #63	+0.55		Not promising
$CaMnSb_2$	Pnma #62	+0.55	2 N sites, 2 Sn sites	Promising

Experimental and calculated XRD patterns are shown in Figure 9. We note that the calculated and experimental XRD patterns differ significantly, and thus we do not believe that the $CuBiS_2$-type structure is entirely correct. However, the DFT electronic structure calculations on the $CuBiS_2$-type structure indicate that it is a semiconductor with a band gap of 1.68 eV and an optical absorption onset not unlike what we observe experimentally (Figure 9 inset). Thus we believe that the space group and local atomic coordination are similar to our candidate structure, but the actual atomic positions require refinement. Further refinement was not possible using this diffraction data: small crystals and crystallographic orientation may still be preventing convergence. Additional challenges may take the form of deviations from SnN stoichiometry arising from nitrogen deficiency and oxygen inclusions.

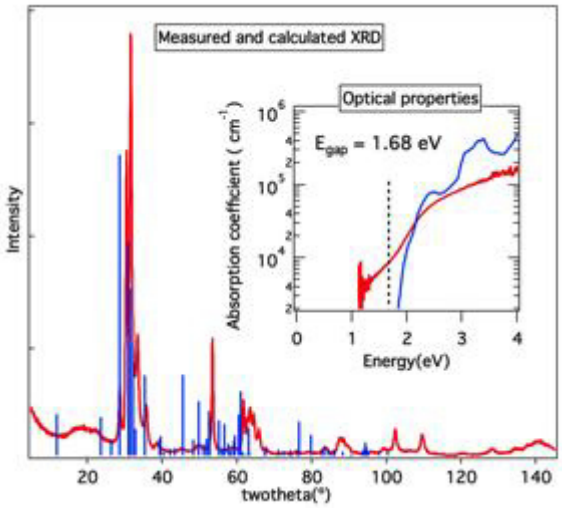

Fig. 4.9: comparison between experimental $SnN_{1-\delta}$ XRD (red) and simulated XRD for $CuBiS_2$-type structure (blue). Inset: Calculated (blue) and experimental (red) optical properties of the same materials.

The discovery of a novel, binary, semiconductor composed of Earth-abundant elements at mild synthesis conditions is exciting for two reasons. First, it demonstrates that the periodic table still holds compounds awaiting discovery. In the group IV nitrides, only the IV_3N_4 materials are known, and nitrides containing Si(II) and Ge(II) may possibly be prepared by this combinatorial sputtering method. Possible uses for this material include optoelectronic energy conversion application such as light emitting diodes, tandem photovoltaics, and photoelectrochemical water splitting, though the structure must be solved and the defect density reduced before practical applications are realizable.

Conclusions

This report details the synthesis, characterization, and structural prediction of SnN1-δ, a novel earth-abundant semiconductor. Structure prototype methods indicate that space group P n m a #62 is likely. Whilst we have made every effort to determine the crystal structure of this material, we must leave atomic position refinement to future work. Larger crystals and fewer defects should assist in crystal structure determination, and would also lead to better understanding of possible uses.

Supplemental information:

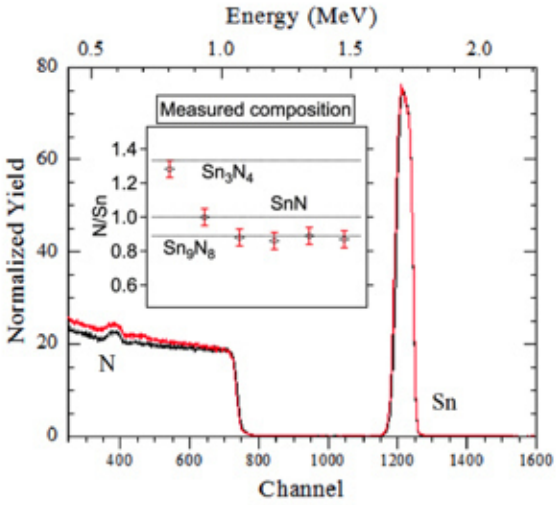

Fig. S4.1: Rutherford backscattering spectrum of tin nitride films. Inset: Measured composition of five $SnN_{1-\delta}$ films grown on silicon and one Sn_3N_4 film for reference.

Modulation of growth conditions did indeed produce difference in XRD patterns. However, the The area detector images in Figure S2 make this clear: All three very different detector images integrate to approximately the same pattern. The presence of the weak peak near 29° in Figure S2 further develops this point: when these films were scrapped to produce a more powder-like sample, the relative intensity of that peak increased dramatically: it can be seen clearly in Figure 2 of the main text. Thus the method of determining phase-purity by modulating growth conditions and observing changes in XRD has limited efficacy: Changes in XRD may simply be changes in crystallographic orientation.

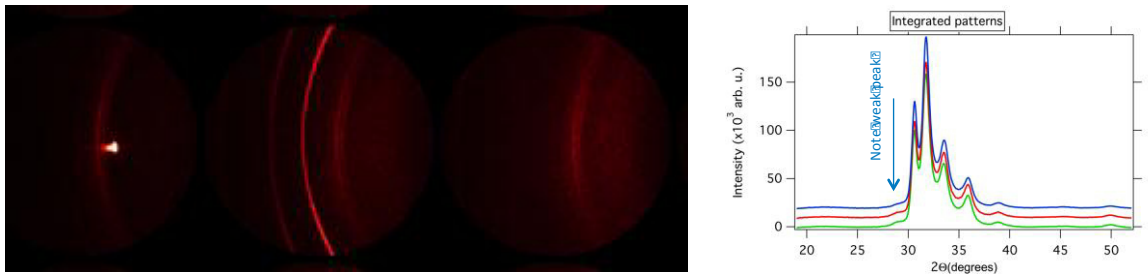

Fig. S4.2: Area detector images (left) and integrated patterns (right) for $SnN_{1-\delta}$ grown at slightly different target-substrate distances.

Table S4.1: X-ray diffraction data for $SnN_{1-\delta}$ powder prepared by scraping films grown on glass

d-spacing (A)	2theta (°) Cu Ka	Intensity	Comments
3.13	28.56	Moderate	Very weak in films
2.94	30.42	Very strong	
2.84	31.52	Very strong	
2.67	33.58	Strong	
2.51	35.74	Moderate	
2.31	38.98	Weak	
2.26	39.90	Very weak	
1.84	49.60	Weak	
1.75	52.42	Strong	
1.56	59.12	Very weak	
1.50	61.70	Moderate	
1.48	62.70	Moderate	Cluster
1.47	63.46	Moderate	
1.45	64.40	Moderate	
1.42	65.88	Moderate	
1.30	72.72	Very weak	
1.25	75.88	Very weak	
1.21	79.50	Very weak	
1.16	83.68	Weak	
1.11	87.62	Moderate	Broad: likely a cluster
1.04	95.88	Very weak	
1.01	99.32	Very weak	
0.99	102.30	Weak	
0.94	109.46	Weak	
0.89	120.14	Very weak	
0.86	128.14	Very weak	
0.82	141.02	Weak	Very broad

Table S2: SEAD lattice spacing values and comparison to possible XRD matches.

d (Å) from SEAD spots	d (Å) from SAED rings	Possible XRD matches
4.6		twice 2.31
3.063	3.051	3.13 or twice 1.50
2.671	2.812	2.67
2.471	2.509	2.51 or twice 1.25
1.719		1.75 or twice 0.86
1.704	1.704	twice 0.86
	1.49	1.48 or 1.50
1.228	1.245	1.25 or 1.21

References

(1) Moreno, F. P. Explorations in Patagonia. *Geogr. J.* **1899**, *14*, 241–269.

(2) Blankenship, L. E.; Yayanos, a. A.; Cadien, D. B.; Levin, L. a. Vertical Zonation Patterns of Scavenging Amphipods from the Hadal Zone of the Tonga and Kermadec Trenches. *Deep Sea Res. Part I Oceanogr. Res. Pap.* **2006**, *53*, 48–61.

(3) Jamieson, a. J.; Fujii, T.; Solan, M.; Matsumoto, a. K.; Bagley, P. M.; Priede, I. G. First Findings of Decapod Crustacea in the Hadal Zone. *Deep Sea Res. Part I Oceanogr. Res. Pap.* **2009**, *56*, 641–647.

(4) Kohshima, S. A Novel Cold-Tolerant Insect Found in a Himalayan Glacier. *Nature* **1984**, *310*, 225–227.

(5) Sloan, R. E.; Van Valen, L. Cretaceous Mammals from Montana. *Science (80-.).* **1965**, *148*, 220–227.

(6) Huber, D.; Carter, J. a; Barbieri, M.; Miglio, A.; Deck, K. M.; Fabrycky, D. C.; Montet, B. T.; Buchhave, L. a; Chaplin, W. J.; Hekker, S.; *et al.* Stellar Spin-Orbit Misalignment in a Multiplanet System. *Science* **2013**, *342*, 331–334.

(7) Tarter, J. THE SEARCH FOR EXTRATERRESTRIAL INTELLIGENCE (SETI). *Annu. Rev. Astron. Astrophys.* **2001**, *39*, 511–548.

(8) Senkan, S. M. High-Throughput Screening of Solid-State Catalyst Libraries. *Nature* **1998**, *394*, 23–26.

(9) Burgess, K.; Lim, H.; Porte, A. M.; Sulikowski, G. A. New Catalysts and Conditions for a C-H Insertion Reaction Identified by High Throughput Catalyst Screening. *Angew. Chem. Int. Ed. Engl.* **1996**, *35*, 220–222.

(10) Reetz, M. T.; Becker, M. H.; Klein, H.-W.; Stockigt, D. Enantioselective Catalysts **. *Ange* **1999**, *28*, 1758–1761.

(11) Aad, G.; Abajyan, T.; Abbott, B.; Abdallah, J.; Abdel Khalek, S.; Abdelalim, a. a.; Abdinov, O.; Aben, R.; Abi, B.; Abolins, M.; *et al.* Observation of a New Particle in the Search for the Standard Model Higgs Boson with the ATLAS Detector at the LHC. *Phys. Lett. B* **2012**, *716*, 1–29.

(12) Birks, J. B. *Rutherford at Manchester*; W. A. Benjamin: New York, 1962.

(13) Disalvo, F. J. Solid-State Chemistry: A Rediscovered Chemical Frontier. *Science* **1990**, *247*, 649–655.

(14) Saal, J. E.; Kirklin, S.; Aykol, M.; Meredig, B.; Wolverton, C. Materials Design and Discovery with High-Throughput Density Functional Theory: The Open Quantum Materials Database (OQMD). *Jom* **2013**, *65*, 1501–1509.

(15) Zakutayev, A.; Zhang, X.; Nagaraja, A.; Yu, L.; Lany, S.; Mason, T. O.; Ginley, D. S.; Zunger, A. Theoretical Prediction and Experimental Realization of New Stable Inorganic Materials Using the Inverse Design Approach. *J. Am. Chem. Soc.* **2013**, *135*, 10048–10054.

(16) McMillan, P. F. New Materials from High-Pressure Experiments. *Nat. Mater.* **2002**, *1*, 19–25.

(17) Kim, C.; Noh, M.; Choi, M.; Cho, J.; Park, B. Critical Size of a Nano SnO2 Electrode for Li-Secondary Battery. *Chem. Mater.* **2005**, 3297–3301.

(18) Noguchi, H.; Setiyadi, A.; Tanamura, H.; Nagatomo, T.; Omoto, O. Characterization of Vacuum-Evaporated Tin Sulfide Film for Solar Cell Materials. *Sol. Energy Mater. Sol. Cells* **1994**, *35*, 325–331.

(19) Walters, P. A. Dentinal Hypersensitivity: A Review. *J. Contemp. Dent. Pract.* **2005**, *6*, 1–10.

(20) Paraskevas, S.; Van Der Weijden, G. A. A Review of the Effects of Stannous Fluoride on Gingivitis. *J. Clin. Periodontol.* **2005**, *33*, 1–13.

(21) ICSD and ICDD Search, 2014.

(22) Scotti, N.; Kockelmann, W.; Senker, J. Sn3N4, Ein Zinn (IV)-Nitrid - Synthese Und Erste Strukturbestimmung Einer Bina È Ren Zinn-Stickstoff-Verbindung. *Z. Anorg. Allg. Chem.* **1999**, *625*, 1435–1439.

(23) Lützenkirchen-hecht, D.; Scotti, N.; Chemie, F.; Dortmund, U. XAFS Investigations of Tin Nitrides. *J. Synchrotron Radiat.* **2001**, *8*, 698–700.

(24) Submaraniyan, A.; Perkins, J. D.; O'Hayre, R. P.; Lany, S.; Stephanovic, V.; Ginley, D. S.; Zakutayev, A. Non-Equlibrium Deposition of Phase Pure Cu2O Thin Films at Reduced Growth Temperature. *APL Mater.* **2014**, *2*.

(25) Caskey, C. M.; Richards, R. M.; Ginley, D. S.; Zakutayev, A. Thin Film Synthesis and Properties of Copper Nitride, a Metastable Semiconductor. *Mater. Horizons* **2014**.

(26) Shemkunas, M. P.; Wolf, G. H.; Leinenweber, K.; Petuskey, W. T. Rapid Synthesis of Crystalline Spinel Tin Nitride by a Solid-State Metathesis Reaction. *J. Am. Ceram. Soc.* **2002**, *85*, 101–104.

(27) Trimarchi, G.; Zunger, A. Global Space-Group Optimization Problem: Finding the Stablest Crystal Structure without Constraints. *Phys. Rev. B* **2007**, *75*, 104113.

(28) Curtarolo, S.; Morgan, D.; Ceder, G. Accuracy of Ab Initio Methods in Predicting the Crystal Structures of Metals: A Review of 80 Binary Alloys. *Calphad* **2005**, *29*, 163–211.

(29) Zhang, X.; Stevanović, V.; D'Avezac, M.; Lany, S.; Zunger, A. Prediction of A2BX4 Metal-Chalcogenide Compounds via First-Principles Thermodynamics. *Phys. Rev. B* **2012**, *86*, 014109.

CHAPTER 5 SYNTHESIS AND PROPERTIES OF ANTIMONY OXYNITRIDE THIN FILMS

Christopher M. Caskey,[1,2] Joshua Ford,[1,3] Ryan M. Richards,[2] Andriy Zakutayev[1]

1) National Renewable Energy Laboratory
2) Colorado School of Mines
3) University of Colorado

This chapter will be submitted to a peer-reviewed journal for publication. The first author was responsible for thin film synthesis, most of the measurements, and manuscript preparation.

Abstract

Metal oxynitrides are diverse group of compounds finding applications from catalysis to microelectronics. Relatively unknown is antimony oxynitride, which we prepare by reactive sputtering and measure its bulk stoichiometry for the first time. The oxynitride thin films have approximate composition $Sb_3O_{3x}N_{5-2x}$, where x is near 0.4. The films are resistive, have an optical absorption onset near 2 eV, and have low long-range order. The stability of the films was found to be dependent on the growth temperature, with films grown at ambient temperature being shelf-stable while films grown at elevated temperatures converted to the oxide. The optical properties suggest that this material is substantially different than antimony oxynitrides reported in the past.

Introduction

Metal oxynitrides are an important class of inorganic compounds because their properties typically range between those of the pure oxide and pure nitride. In many cases oxynitrides maintain the favorable properties from each class: In general, oxynitrides have increased covalent bonding character compared to the corresponding oxide due to the lower electronegativity of nitrogen compared to oxygen. Conversely, oxynitrides typically demonstrate increased thermodynamic stability compared to the pure nitride because of the higher reactivity (lower bond strength) of molecular oxygen compared to molecular nitrogen. Oxynitrides often possess semiconducting band structure, and because their conduction band maxima are frequently made up of anion p orbitals, the absolute energy difference between O p and N p

orbitals can be exploited to produce tunable properties.[1,2] Oxynitrides find a wide range of applications: silicon oxynitride is used by the semiconductor industry as a dielectric gate material in microelectronics,[3] and has been investigated as a phosphor material for light-emitting diodes.[4] Addition of nitrogen to oxide glasses leads to improved mechanical properties,[5] and aluminum oxynitride and can used as a infrared-visible window material.[6] Oxynitrides of Ti and Ta have been used as absorbers in water splitting cells, offering a decreased band gap compared to the oxides.[7] Oxynitrides are also used in catalysis: aluminophosphate oxynitrides and silicon oxynitrides are solid base catalysts capable of driving condensation reactions,[8,9] and various metal oxynitrides have been explored as replacements for platinum in the cathode of polymer electrolyte membrane fuel cells.[10]

Antimony oxide (Sb_2O_3) is a well-known compound used industrially as a component in flame-retardants and as a catalyst for ethylene polymerization. Much of the worldwide production of antimony (in excess of 160,000 tons annually) becomes Sb_2O_3 for these applications.[11,12] The corresponding nitride is much less known. Researchers have assigned gas-phase spectra of SbN dimers,[13–15] a solid-state antimony nitride measured by XPS as Sb_3N was investigated as an anode material for lithium ion batteries,[16] and transparent, amorphous antimony nitride obtained by chemical vapor deposition has been reported.[17] Reports of antimony oxynitride are scarcer still, with publications limited to patents regarding its use as a ultraviolet absorbing layer in windows[18] and as a resistive material in a bolometer.[19] All of the solid-state reports of antimony nitride and antimony oxynitride lack reliable quantification of the bulk stoichiometry, leaving it unclear what the true natures of these films are.

We report the synthesis and characterization of antimony oxynitride thin films with approximate composition $Sb_3O_{3x}N_{5-2x}$, where x is near 0.4. The films are resistive, have low long-range order, and have an optical absorption onset near 2 eV. The stability of the films was found to be dependent on the growth temperature.

Methods

Thin films of antimony oxynitride were synthesized by radio-frequency (RF) reactive sputtering of a 2 inch antimony metal target in a nitrogen and argon atmosphere. The partial pressure of argon and nitrogen were each 10 mTorr, and the incorporated oxygen originated from the base pressure gasses (mostly H_2O) present at $2.1*10^{-6}$ Torr or less. The nitrogen was sourced through an RF atom source, and the glass and silicon substrates were affixed to a heater on one

end with the other suspended in vacuum, leading to a temperature gradient across the sample.[20] Power supplied to the Sb target was 20 W, and power supplied to the RF atom source was 250 W. After growth, Rutherford backscattering (RBS), cross-plane electrical conductivity, kelvin probe, ultraviolet-visible spectroscopy, and X-ray diffraction (XRD) were used to characterize films. Analysis of RBS spectra was conducted using the PERT simulation function in the Rutherford Universal Modeling Package (RUMP).

Results and Discussion

RBS analysis was preformed on a film grown at ambient temperature on single-crystal silicon. The stoichiometry was determined to be $SbO_{0.4}N_{1.4}$. The RBS spectrum is shown in Figure 1. The films have very low electrical conductivity: cross-plane resistivity measurements of a 300 nm film grown at ambient temperature on fluorinated-tin oxide-coated glass showed resistivity over 20 MΩ, putting the bulk resistivity of Sb-O-N at least 10^{11} Ωcm. The measured work function of this film was 5.1 eV. Optical characterization of films grown at ambient temperature showed complete absorption at wavelengths shorter 500 nm with a steep increase in transmission at longer wavelengths. Above 750 nm, films were almost entirely transparent. The reflection-corrected transmission of a film grown at ambient temperature is shown in Figure 2.

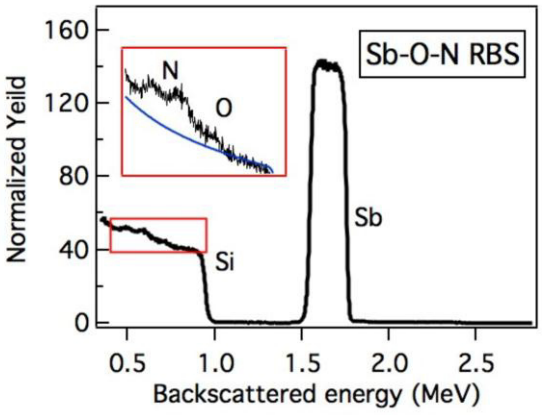

Fig. 5.1: Rutherford backscattering spectrum of antimony oxynitride film grown at ambient temperature on silicon. Inset: Enlargement of anion signal (black) with simulated silicon background (blue).

The results suggest an optical band gap near 2 eV, which is 0.8-1.8 eV lower than earlier reports of antimony oxynitride[18] and antimony nitride.[17] Differences in anion content or metal oxidation state are likely responsible for the difference in optical properties: Reasoning solely by the

frequently-observed reduction in band gap for nitrides compared to oxides, it appears we may have prepared a more nitrogen-rich material than previous studies. However, the metal oxidation state can also play a role, with Sb_2O_4 and Sb_2O_5 having smaller band gaps than Sb_3O_2.[21] It is unusual for a disordered material with an apparently moderate band gap to display such high

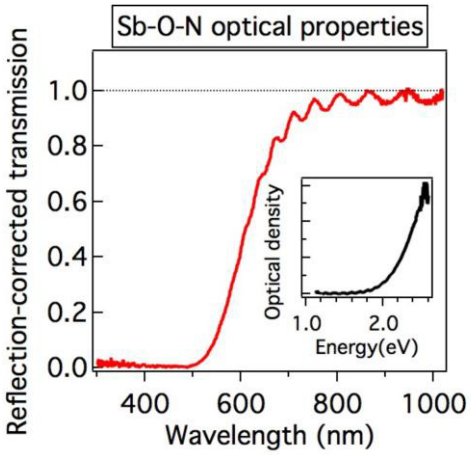

Fig. 5.2: Optical properties of Sb-O-N film approximately 2.3 μm thick synthesized at ambient temperature. Inset: dimensionless absorption coefficient as a function of photon energy.

resistivity. The low conductivity could originate from a very low carrier concentration or from extremely low carrier mobility, and either explanation implies something peculiar about the electronic structure. The numeric results for films grown at ambient temperature are summarized in Table 1.

Table 1: Results obtained for Sb-O-N films grown at ambient temperature.

Stoichiometry	Resistivity	Work Function	Optical absorption onset
$SbO_{0.4}N_{1.4}$	$>10^{11}$ Ωcm	5.1 eV	2 eV

As synthesized, the stoichiometry $SbO_{0.4}N_{1.4}$ (measured on films grown at ambient temperature) suggests that antimony incorporates as Sb(V). Increasing the substrate temperature produces more reducing film growth conditions, and Sb(0) metal is observed in the XRD for films synthesized at 350°C. The amorphous films grown just below 350°C were likely also reduced compared to the films grown at ambient temperature. These reduced films were more

prone to conversion to the crystalline oxide than the films grown at lower temperatures. When stored in atmosphere, initially red, amorphous films slowly converted to clear, crystalline material. The films grown at the highest temperatures were the first to turn clear, and the change progressed along a front from higher growth temperature to lower growth temperature. The crystallographic transformation is shown in Figure 3. Films grown at ambient temperature have not (after over three months of storage) changed visually or crystallographically.

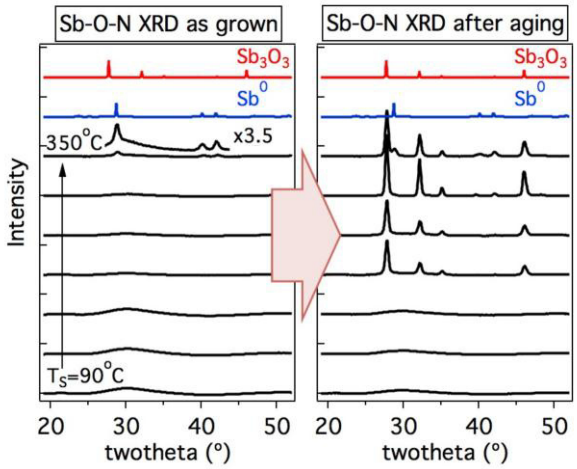

Fig. 5.3 left: XRD patterns of films grown at different substrate temperatures. Fig. 5.3 right: XRD patterns of the same films after 100 days of shelf-storage.

To investigate the thermal stability of the films grown at ambient temperature, we preformed a high-throughput annealing experiment. We affixed one end of the sample to a heater with conductive paste, leaving most of the sample suspended in vacuum (20 mtorr of N_2 & Ar.) This produced a temperature gradient across the sample. Annealing at high temperatures (400-450°C) led to decomposition of the amorphous oxynitride material and crystallization of antimony oxide (Sb_2O_3). Some amorphous content remained, but no XRD peaks indicative of a crystalline nitride or oxynitride phase were observed. This high-temperature region was grey in color suggesting antimony metal, but no metallic peaks were observed in the XRD, and the films were resistive. We therefore hypothesize that some oxygen and nitrogen remained bound to the antimony in an amorphous matrix. X-ray diffraction data and a photograph of the sample are shown in Figure 4.

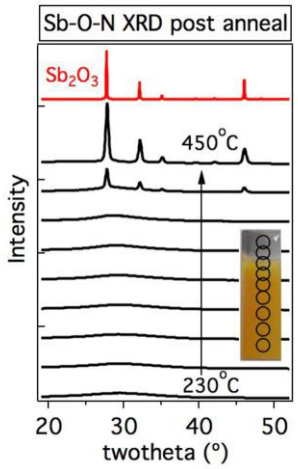

Fig. 5.4: XRD patterns of Sb-O-N films annealed at various temperatures in nitrogen and argon atmosphere. Inset: Photograph of annealed sample with circles indicating points sampled by XRD.

The fact that crystalline Sb-O-N phases were not observed in either high-substrate temperature depositions or in annealing of room temperature deposited films suggests that no high-stability structure exists in this materials system. Pure nitrides (SbN or Sb_3N_5) are also not likely to be highly stable materials, as they were also not observed. However, crystalline nitride phases may still be obtainable by excluding oxygen further through reducing the base pressure of the deposition chamber.

Conclusions

Antimony oxynitride, $SbO_{0.4}N_{1.4}$, was grown at room temperature by reactive sputtering. These films appear to be shelf-stable and are thermally stable in inert atmosphere below ~400°C. The films had an optical absorption onset near 2 eV, which is lower in energy than observations in previous studies of antimony nitrides and oxynitrides. More reduced films were grown at increased temperature, and these films converted to Sb_2O_3 in atmosphere. Open areas of research include the origin of the high resistivity of the films, which could be caused by the presence of very few carriers or very low carrier mobility do to a peculiarity of the electronic structure.

References

(1) Marchand, R.; Tessier, F.; Le Sauze, A.; Diot, N. Typical Features of Nitrogen in Nitride-Type Compounds. *Int. J. Inorg. Mater.* **2001**, *3*, 1143–1146.

(2) Ishara, A.; Lee, K.; Doi, S.; Mitsushima, S.; Kamiya, N.; Hara, M.; Domen, K.; Ota, K. Tantalum Oxynitride for a Novel Cathode of PEFC. *Electrochem. Solid-State Lett.* **2005**, *8*, A201–A203.

(3) Green, M. L.; Gusev, E. P.; Degraeve, R.; Garfunkel, E. L. Ultrathin (<4 Nm) SiO2 and Si–O–N Gate Dielectric Layers for Silicon Microelectronics: Understanding the Processing, Structure, and Physical and Electrical Limits. *J. Appl. Phys.* **2001**, *90*, 2057.

(4) Xie, R.-J.; Hirosaki, N. Silicon-Based Oxynitride and Nitride Phosphors for White LEDs—A Review. *Sci. Technol. Adv. Mater.* **2007**, *8*, 588–600.

(5) Hampshire, S. Oxynitride Glasses, Their Properties and Crystallisation – a Review. *J. Non. Cryst. Solids* **2003**, *316*, 64–73.

(6) Corbin, N. D. Aluminum Oxynitride Spinel: A Review. *J. Eur. Ceram. Soc.* **1989**, *5*, 143–154.

(7) Walter, M. G.; Warren, E. L.; Mckone, J. R.; Boettcher, S. W.; Mi, Q.; Santori, E. A.; Lewis, N. S. Solar Water Splitting Cells. *Chem. Rev.* **2010**, *110*, 6446–6473.

(8) Climent, M. J.; Corma, A.; Forn, V.; Frau, A.; Guil-l, R. Aluminophosphates Oxynitrides as Base Catalysts : Nature of the Base Sites and Their Catalytic Implications. *J. Catal.* **1996**, 392–398.

(9) Xia, Y.; Mokaya, R. Highly Ordered Mesoporous Silicon Oxynitride Materials as Base Catalysts. *Angew. Chemie* **2003**, *115*, 2743–2748.

(10) Chen, Z.; Higgins, D.; Yu, A.; Zhang, J. A Review on Non-Precious Metal Electrocatalysts for PEM Fuel Cells. *Energy Envirnomental Sci.* **2011**, *4*, 3167–3192.

(11) Anderson, C. G. The Metallurgy of Antimony. *Chemie der Erde - Geochemistry* **2012**, *72*, 3–8.

(12) *Mineral Commodity Summaries 2014*; 2014.

(13) Ciach, S. Absorption Spectrum of SbN. *J. Chem. Phys.* **1970**, *53*, 3381.

(14) Coy, N. H.; Sponer, H. Emission Spectrum of Antimony Nitride. *Phys. Rev.* **1940**, *58*, 709–713.

(15) Coy, N. H.; Sponer, H. Evidence of a Band System in Antimony Nitride. *Phys. Rev.* **1938**, *53*, 495.

(16) Sun, Q.; Li, W.-J.; Fu, Z.-W. A Novel Anode Material of Antimony Nitride for Rechargeable Lithium Batteries. *Solid State Sci.* **2010**, *12*, 397–403.

(17) Shiraishi, T.; Yasuyuki, A.; Yamazaki, S. Optical and Electrical Properties on Transparency a-SbN Films. *J. Non. Cryst. Solids* **1985**, *77& 78*, 1313–1316.

(18) Lu, Y.; Varaprasad, D. V.; Vanderploeg, J. A. Coated Article with Oxides And/or Oxynitrides of Antimony And/or Zinc Dilectric Layer(s) and Corresponding Method. US 7,695,785 B2, 2010.

(19) Yang, W. S.; Cheon, S. H.; Cho, S. M.; Choi, C. A. Resistive Material for Bolometer, Bolometer for Infrared Detector Using the Material, and Method of Manufacturing the Bolometer. US 8,142,597 B2, 2012.

(20) Subramaniyan, A.; Perkins, J. D.; O'Hayre, R. P.; Lany, S.; Stevanovic, V.; Ginley, D. S.; Zakutayev, A. Non-Equilibrium Deposition of Phase Pure Cu2O Thin Films at Reduced Growth Temperature. *APL Mater.* **2014**, *2*, 022105.

(21) Allen, J. P.; Carey, J. J.; Walsh, A.; Scanlon, D. O.; Watson, G. W. Electronic Structures of Antimony Oxides. *J. Phys. Chem. C* **2013**, *117*, 14759–14769.

CHAPTER 6 CONCLUSIONS & FUTURE WORK OR: GREAT NEW IDEAS UNDIMMED BY THE CHALLENGES OF ACTUALLY TRYING THEM

The metastable semiconductors described in this dissertation display diverse and interesting properties. Cu_3N may possess defect tolerance, and our study of it produced anion activity modulation and insights into the synthesizability of metastable systems. In our study of tin nitride and the IV_3N_4 polymorphs, we theoretically predict large hole effective masses and small electron effective masses for Sn_3N_4 and suggest that any future use of tin nitride should take advantage of it's potentially very mobile electrons. Chapter 4 details the discovery of a new member of the tin nitride family, $SnN_{1-\delta}$. This is an entirely new material and its structure and uses have not yet been established. Antimony oxynitride, as we have synthesized it, is also likely a new material. At the very least the report in Chapter 5 is the first report of an antimony nitride or oxynitride with reliable characterization of the bulk composition. All of this work is thematically connected by bring new applications to existing materials and bringing new materials to the collective knowledge.

As with any fruitful research, many questions were raised and the many avenues of future research remain which merit exploration. Below is a compilation of potential future work as well as ideas and musings about new techniques.

A method for solving the structure of $SnN_{1-\delta}$

Solving the structure of the $SnN_{1-\delta}$ would dramatically increase the quality and impact of the discovery described in Chapter 4. Detailed here is a proposal to do just that. There are two important pieces of the puzzle which need to be addressed. The first is producing larger crystals, and the second is accurately determining the stoichiometry.

Production of larger crystals could be accomplished by in several ways:

1) Increasing the adatom mobility to encourage crystal growth could be accomplished by increasing the substrate temperature. However, the chemical potential of nitrogen must remain in the proper region to favor $SnN_{1-\delta}$ over Sn_3N_4 and Sn^0. Therefore, the atomic

nitrogen source could be turned on or the partial pressure of nitrogen increased to offset the loss in chemical potential from the raise in temperature.

2) Decreasing the growth pressure or decreasing the target-substrate distance could increase adatom mobility by increasing energetic flux to the substrate. We note that the film appears to adopt a zone 1 or zone T microstructure,[1] which are mobility-limited structures. This microstructure is shown in Figure 4 Chapter 4.
3) Increase grain size through epitaxial growth. If some assumptions are made about the space group, a lattice constant can be hypothesized, and single-crystal substrates may be available.
4) Increase grain size by reducing oxygen inclusions. In the new nitrides chamber, a lower base pressure would lower oxygen contamination of the film. Oxygen-rich grain surfaces could be suppressing coalescence in the current growth.

Accurate determination of the stoichiometry may not be known until the structure is solved, but an assumption is necessary to solve the structure. The amorphous material observed between grains may deviate compositionally from the material incorporated into crystals. Nitrogen is very difficult to measure in RBS, but RBS is one of the only bulk spectroscopic techniques capable of measuring N at all. Alternatives are mass balance experiments after thermal decomposition (such as thermogravimetric analysis). The stoichiometry could also be determined by assuming that all incorporated nitrogen is in the 3- state and that tin is present to balance. The relative quantities of Sn(II) and Sn(IV) can be measured by Mossbauer spectroscopy, and the nitrogen content be determined by charge-balancing. This technique unfortunately does not take into account the contribution of any amorphous material between grains, and is therefore subject to error.

First-principals theory also provides routes to determine structure. The structure prototypes method, which was successful in ABX_2 compounds, could also be applied to AX compounds, A_9X_8 compounds, and $A_6B_3X_8$ compounds. We could also apply First-Principals Assisted Structure Solution (FPASS)[2] to $SnN_{1-\delta}$. Though these techniques are unlikely to solve the structure on their own, in combination with larger-grained films and data from other techniques, structure determination may be successful.

Additionally, the list of possible space-groups can be reduced by knowing the number of unique tin sites in the compound. ^{119}Sn magic-angle spinning nuclear magnetic resonance spectroscopy (MAS NMR) of isotopically enriched $SnN_{1-\delta}$ material can accomplish this. ^{119}Sn-enriched powder can be purchased from American Elements and hot-pressed to the face of a non-enriched target. Contact Brenden Ortiz for hot-pressing. Chai Engtrakul and Erica Gjersing are excited about the project and would be enthusiastic about helping. Our current pulse utilizes a 30 second relaxation time, 14 kHz spinning speed. Useful tin NMR literature is available in the references at the end of this section.[3–5] This technique has the advantage of being more sensitive to crystalline material than it is to amorphous material.

$SnN_{1-\delta}$ TEM & electron diffraction

Another method for producing material which can be analyzed by electron diffraction is to grow very thin $SnN_{1-\delta}$ directly on TEM grids. Some of the crystallites will nucleate on the holey/lacey carbon and be available for TEM & electron diffraction. Chilan Ngo at UCLA has been incredibly helpful in this area and has requested larger crystals for selected-area electron diffraction.

Demonstration of defect tolerance in Cu_3N

A driving hypothesis in the Ternary Copper Nitrides project was defect tolerance, the ability of a material to resist electrical property changes in spite of physical defects. this hypothesis would be tested if we could:

1) Demonstrate the functional relationship of carrier mobility on carrier concentration by Hall measurements on patterned samples. If the mobility is independent of carrier concentration or the mobility is weakly dependent on carrier concentration, this would support the defect-tolerant hypothesis.

2) Demonstrate passivated surfaces by polishing single crystals of Cu_3N and physically linking them in a circuit. After the grains are physically connected, perform impendence spectroscopy to measure the equitant circuit and see what role grain boundaries play. If the inclusion of grain boundaries does not introduce additional resistance in the circuit, the defect

tolerance hypothesis will be supported. On the other hand, the defect tolerance hypothesis will be undermined if the grain boundaries are found to add significant resistance to the circuit.

Figure 6.2 Scheme of Cu_3N crystals as circuit components to test defect tolerance hypothesis

Crystalizing antimony nitride

Antimony nitride, SbN, is expected to crystalize with an enthalpy of formation of 1.1 eV. The presence of small amounts of oxygen could frustrate crystallization, and growing at a lower oxygen partial pressure could reduce the effect. This can be accomplished either by presputtering getter material (Sb, Ti) in Argon/low flow of N_2 or using lower base pressure system. Using a combi temperature gradient during growth or annealing after growth could also encourage crystallinity.

Group IV oxynitrides

Silicon, germanium, and tin show interesting polymorphism in their nitrides (see Chapter 3). Silicon oxynitride is (or at least has been) used industrially in as a gate layer in metal oxide semiconductor field effect transistors (MOSFETS). Tin oxynitride has not been observed but Pawel Zawadzki has some calculations on them, and experimental synthesis would be a nice addition to the story. A literature review on the group IV oxynitrides would be illuminate open questions and possible directions.

Making amorphous tin oxynitride should be quite easy in Combi 1. Indeed, oxygen incorporation is already observed in crystalline tin nitride, and doubtless would be enhanced in the low chemical potential of nitrogen growth conditions that occur at longer target substrate distances. Sn-O-N materials could be made by in three manners. Manner 1 is to flow oxygen, nitrogen, and argon into the sputter chamber. The oxygen flow rate would probably need to be much lower than the nitrogen flow rate, and it may be beneficial to crack the nitrogen with the RF atom source as well. Manner 2 is to cosputter a tin metal target and a tin oxide target in a nitrogen and argon atmosphere. In the (admittedly unlikely) best-case scenario, there would be

an anion composition gradient across the sample. More likely the nitrogen-to-oxygen ratio would depend on the relative powers applied to the two targets, as reactive oxygen species produced at the tin oxide target would quickly find their way to the metal target. In other words, rapid gas-phase equilibrium would trump kinetic, flight-path considerations.

One possible way to produce an anion gradient would be to cosputter from a nitride target and an oxide target in a relatively low base pressure. We have both Si_3N_4 and SiO_2 targets available now. The gas-phase mixing could be discouraged by the low pressure: few collisions from which one anion species could be directed to the alternative target. Another method would be to use a semi-mask technique wherein a physical barrier is imposed between the cosputtering targets. This barrier would end some distance from the target (an obvious need for optimization is the distance) and would permit limited gas-phase mixing on the way to the substrate. In Combi-1, this barrier could be simply and reversibly attached to the pop-up valve or underside of the lid. It is noteworthy that such geometry may constrain the effectiveness of the atomic nitrogen source.

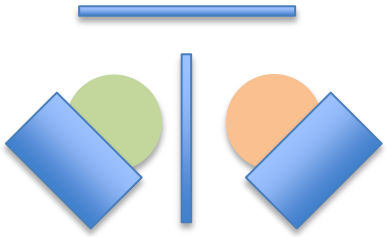

Figure 6.3 Schematic of combinatorial sputtering apparatus to produce anion composition gradients

Amorphous copper tin nitride

Copper nitride is interesting in that it presents a relatively shallow work function. Tin nitride is fascinating for its band gap in the visible and both are interesting for their Earth-abundant composition. In the ternary Cu-Sn-N system, a large composition space between Cu_3N and Sn_3N_4 exists where sputtered films have low structural order. The semiconducting properties of this amorphous material appear to smoothly span the property space between the two binaries. Further investigation of this material may lead to tunable semiconducting properties.

The Paper on a Wafer

First and foremost, this idea needs a better name. Publication Station? Results Square? It's not really a wafer, so…Something Glass?

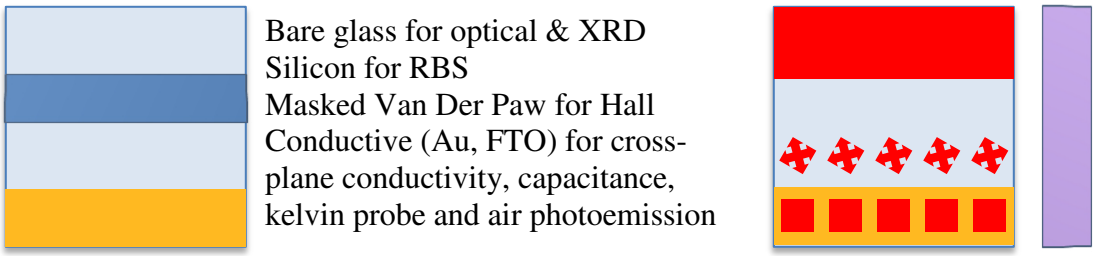

Figure 6.4 Schematic of glass slide modified for facile accurate measurements of single-gradient sample libraries.

Sb-O-N NMR

Additional structural information about antimony oxynitride may be obtainable by MAS-NMR. ^{121}Sb is an MNR active nucleus with spin 5/2. This would probably lead to severe broadening but the abundance over 50% and the growth rate quite high so adequate quantities of material could be produced readily. The high abundance could present an additional difficulty as spin-spin splitting could further broaden lines.

After consulting with coworkers, some of these ideas will be undertaken during fall of 2014. Others may wait for future researchers.

References

(1) Thornton, J. A. The Microstructure of Sputter-Deposited Coatings. *J. Vac. Sci. Technol. A* **1986**, *4*, 3059–3065.

(2) Meredig, B.; Wolverton, C. A Hybrid Computational-Experimental Approach for Automated Crystal Structure Solution. *Nat. Mater.* **2013**, *12*, 123–127.

(3) Clayden, N. J.; Dobson, C. M.; Fern, A. High-Resolution Solid-State Tin-119 Nuclear Magnetic Resonance Spectroscopy of Ternary Oxides. *J. Chem Soc Dalt. Trans.* **1989**, 843–847.

(4) Cruz, L. P.; Savariault, J.; Rocha, J.; Jumas, J.; Jesus, J. D. P. De. Synthesis and Characterization of Tin Niobates. *J. Solid State Chem.* **2001**, *156*, 349–354.

(5) Mundus, C.; Taillades, G.; Pradel, A.; Ribes, M. A 119 Sn Solid-State Nuclear Magnetic Resonance Study of Crystalline Tin Sulphides. *Solid State Nucl. Magn. Reson.* **1996**, *7*, 141–146.

APPENDIX I: PROCEDURES & CALIBRATIONS

This appendix is intended to provide additional procedural notes to assist with any future repetition of the results contained in this dissertation. The

Combi-1

Combi-1 is a custom-built combinatorial sputtering tool used for oxides and nitrides. It contains three radio-frequency (RF) power supplies and 4 gun positions. One gun position is frequently occupied with the RF atom source. Specific safety and tool-level procedures are contained in the Equipment Specific Procedures on file in the lab. However, some procedures specific to nitrides are delineated below.

The atomic nitrogen source must be lit prior to the other guns in order to ensure that the plasma lights. This is confirmed visually through the view window by the presence of a very faint glow from the interior of the source. Gas flow to the source is controlled through a needle valve, which is calibrated against mass-flow controllers. In order to calibrate the needle valve, the pump throttle valve is left in one position and the needle valve is opened (or closed) in increments. At each valve position, the pressure is allowed to equilibrate and the pressure recorded, producing a functional relationship between pressure and valve position. This process is repeated using a mass flow controller (calibrated by the manufactured, MKS) producing a functional relationship between flow rate and pressure. The two relationships can then be combined to elucidate the flow rate from the needle valve at each valve position.

For the atomic gas source, the typical operating power setting is 250 W. Though the source is designed to use powers above 500 W, in practice the source becomes extremely hot at powers above 300 W, as the cooling appears to be insufficient to keep up with heat generation.

The temperature at each point on the glass substrate is one of the variables in our process with a high degree of uncertainty. The temperature was calibrated by placing a thermocouple (affixed with silver paste) on the substrate at various distances from the heater contact. The heater was turned on, the temperature allowed to equilibrate, and the temperature recorded. This was repeated at many points on the surface. The initial calibrations were done at atmospheric pressure, and a small number of the points were repeated at deposition pressure (20 mTorr) to

check the pressure dependence. To check for heater drift, a thermocouple was attached to the front side of the sample in about 10% of depositions.

Metrology

After films have been prepared, they undergo various types of metrology. Standard for most films is X-ray diffraction (XRD), X-ray fluorescence (XRF), and optical spectroscopy. Also used on select samples is four-point probe, scanning electron microscopy, Hall effect measurements, Rutherford backscattering (RBS), and electron microscopy. The XRD tools are aligned by NREL staff, but testing the alignment with known samples is beneficial from time to time. The XRF tools used in thesis are not currently functioning, though they were calibrated using high-purity reference materials. The thickness measurements used in this dissertation come from two sources: XRF measurements and profilometry measurements. The XRF thicknesses cannot be considered accurate without the corroboration of profilometry measurements, which are referenced to known samples. Any future measurements should be made with the system in Solar Energy Research Facility room C112.

APPPENDIX II: COAUTHOR PERMISSIONS

I, Ryan Richards grant Christopher Caskey permission to use the paper *Thin-film synthesis and properties of copper nitride, a metastable semiconductor* in his doctoral dissertation

I, Andriy Zakutayev grant Christopher Caskey permission to use the paper Thin-film synthesis and properties of copper nitride, a metastable semiconductor and other papers published in collaboration with Chris in his doctoral dissertation